Hindawi
Geofluids
Volume 2017, Article ID 4292079, 23 pages
https://doi.org/10.1155/2017/4292079

Research Article

Diagenetic Heterogeneity of Deep Sandstones and Its Relationship to Oil Emplacement: A Case Study from the Middle Jurassic Toutunhe Formation in the Fukang Sag, Central Junggar Basin (NW China)

Binfeng Cao,[1,2] Xiaorong Luo,[1,2] Likuan Zhang,[1] Fenggui Sui,[3] Huixi Lin,[3] and Yuhong Lei[1]

[1]*Key Laboratory of Petroleum Resources Research, Institute of Geology and Geophysics, Chinese Academy of Sciences, Beijing 100029, China*
[2]*University of Chinese Academy of Sciences, Beijing 100049, China*
[3]*Institute of Western Frontier Area, Shengli Oilfield Company, SINOPEC, Dongying 257000, China*

Correspondence should be addressed to Binfeng Cao; cao_binfeng@126.com

Received 4 March 2017; Accepted 27 June 2017; Published 25 September 2017

Academic Editor: Stefano Lo Russo

The Middle Jurassic Toutunhe Formation at depths of approximately 4000–6000 m has increasingly come into focus as a current deep reservoir target in the central Junggar Basin (NW China). Based on petrography, SEM, stable isotopes, and fluid inclusion analyses, the goals of this study were to investigate the effect of depositional lithofacies on sandstone diagenetic heterogeneity and to examine the relationship between diagenetic evolution and oil charge within a heterogeneous reservoir. Grain size controls the overall abundance of cement and porosity and reservoir properties through its effect on ductile lithic sand grains and hence on mechanical compaction. Early diagenetic calcite cement is an exception to this trend. Ductile lithic-rich, very fine-grained sandstones featured compaction of easily deformed, clay-rich grains, resulting in a very rapid loss of porosity during burial. In contrast, dissolution and cementation occurred as well as ductile compaction in the fine-grained sandstones. Two episodes of oil charge occurred in the relatively coarser-grained sandstone lithofacies. Diagenesis progressed alternately with oil emplacement, and some diagenetic alterations and oil charge occurred simultaneously. Ductile lithic-rich, highly compacted sandstones and tightly calcite-cemented sandstones can create permeability barriers embedded in permeable reservoir sandstones, probably resulting in heterogeneous flow.

1. Introduction

Reservoir heterogeneity refers to spatial variability of a system property (e.g., porosity, permeability, and pore structure) at a specified scale [1–4]. The intrinsic complexity of a reservoir is the result of various geological processes, including depositional environment, diagenesis, and tectonic imprint. The heterogeneity is a critical factor affecting fluid flow and distribution within a reservoir [5, 6]. Diagenetic studies that are pertinent to reservoir characterization have been confined almost entirely to the identification and quantification of mineral components and porosity types by combined use of scanning electron microscope (SEM) and thin section and surely do not characterize diagenetic heterogeneity, especially at scales larger than microscopic scale. The primary texture and detrital compositions of sandstones, sand body geometry, and architecture, ultimately controlled by depositional environment, are of decisive importance in determining the rate and pathways of fluid flow affecting the extent and distribution of early diagenetic alterations in sandstones [7–12]. Early diagenesis in turn exerts a substantial control on the deep-burial diagenetic evolution of the sandstones [9, 10, 13]. It seems plausible that a significant component of sandstone diagenetic heterogeneity arises from initial variations in texture and grain compositions in principle [8, 14]. Thus, linking diagenetic alterations to depositional environments

and lithofacies has been an important concept for evaluating a degree of large-scale heterogeneity characterizing diagenetic features [9, 10]. This is essential to achieve a complete and adequate spatial representation of a heterogeneous reservoir.

Hydrodynamic fluctuations and varying depositional facies associations directly determine textural and compositional parameters of sandstone sediments, producing differential compaction and diagenetic processes, as well as reservoir quality evolutions [15–17]. Some sandstone lithofacies have experienced a very rapid loss of porosity through compaction or cementation and have achieved a high capillary entry pressure during early diagenesis and have acted as low-permeability barriers to late fluid (hydrocarbons included) flow in a reservoir [17–19]. However, studies of differential sandstone diagenesis and porosity evolutions at a reservoir scale level are still far from being fully explored in the literature.

In recent years, the Jurassic lithologic and stratigraphic traps have become a major focus of deep reservoir exploration in the central Junggar Basin (NW China). Some oil fields such as Mobei, Mosuowan, and Moxizhuang oil fields have been discovered in the Jurassic sandstones (Figure 1(a)), reflecting promising prospects for deep exploration. No significant discoveries have been obtained in the Fukang Sag. By the end of 2014, the Shengli Oilfield Company, SINOPIC, has completed seven wells in this area (Figure 1(b)) and has obtained substantial findings in the Lower-Middle Jurassic sandstones. The recoverable oil original reserves were estimated to be approximately 2109.35×10^4 t (155 million bbl). The focus of this study is the Middle Jurassic Toutunhe Formation (Figures 2 and 3). This formation is buried at depths of approximately 4000–6000 m. The sandstones have strongly heterogeneous petrophysics with porosities of 2.1–16.4% and permeabilities of 0.02–28.9 mD. The inhomogeneity of oil shows has been noted from core description, well logs to well tests. The aim of the study is to investigate the effect of depositional environments and lithofacies on sandstone diagenetic heterogeneity and to decipher the diagenetic evolution pathways of a heterogeneous reservoir and its impact on hydrocarbon migration.

2. Geological Setting

The Fukang Sag is located in the Junggar Basin, which covers an area of approximately 136,000 km^2 (52,509 mi^2) north of Xinjiang Uygur Autonomous Region, northwest China (Figure 1(a)). The Junggar Basin is triangle-shaped and is confined by the Qinggelidi and Kelameili Mountains to the northeast, by the Yilinheibiergen and Bogda Mountains to the south, and by the Zhayier and Halalate Mountains to the northwest. The basin lies at a three-block junction between Kazakhstan, Siberia, and Tarim and is a part of the Kazakhstan block [20]. The Junggar Basin is floored by Precambrian crystalline basement and part of Hercynian folded basement [21] and is an Upper Paleozoic, Mesozoic, and Cenozoic superimposed basin. The basin has experienced the Hercynian, Indosinian, Yanshanian, and Himalaya orogenies. Three main phases of deformation have been recognized in the basin: the Middle-Late Permian rift stage, Triassic to Paleogene depression

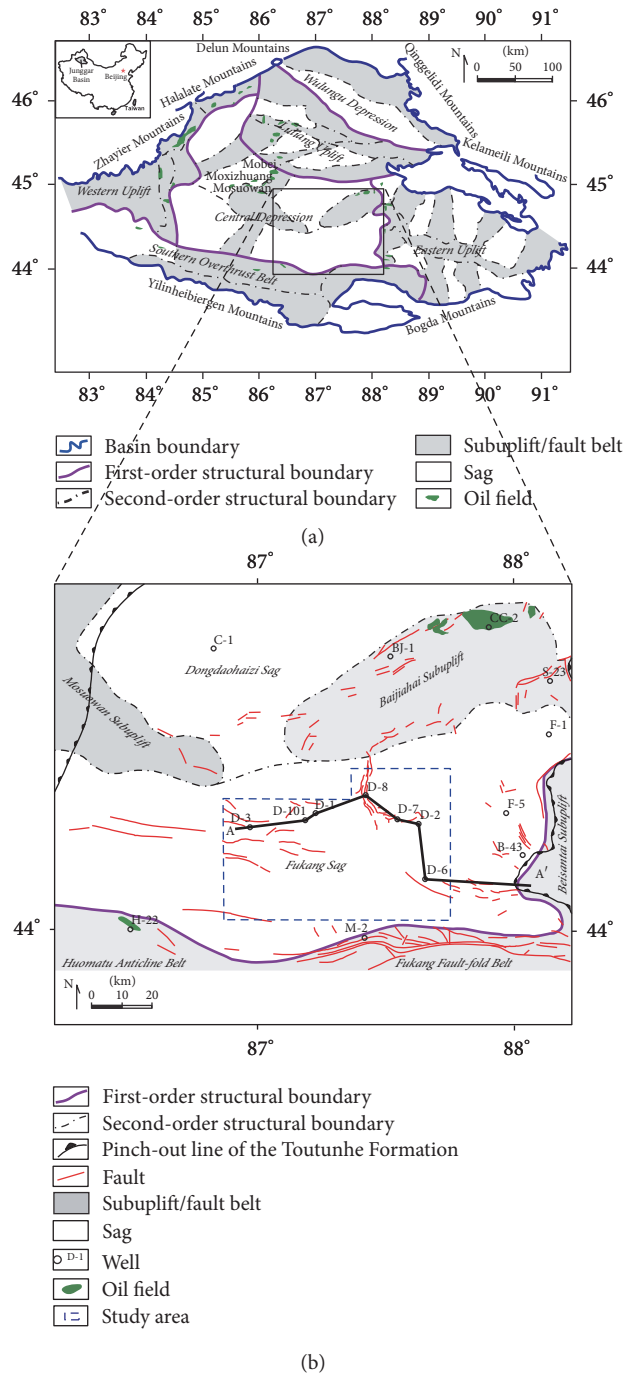

FIGURE 1: (a) Regional geological map showing structural features of the Junggar Basin and location of the study area [24]. (b) Location of the studied wells.

stage, and Neogene to Quaternary foreland stage [22, 23] (Figure 3). The Junggar Basin contains six structural units: the Wulungu Depression, Luliang Uplift, Western Uplift, Central Depression, Southern Overthrust Belt, and Eastern Uplift [24]. Each structural unit has a distinct structural style and tectonic history. The Fukang Sag lies in the Central Depression (Figure 1(b)). The main structure within the sag is a northeast-southwest trending monocline (Figure 2), which

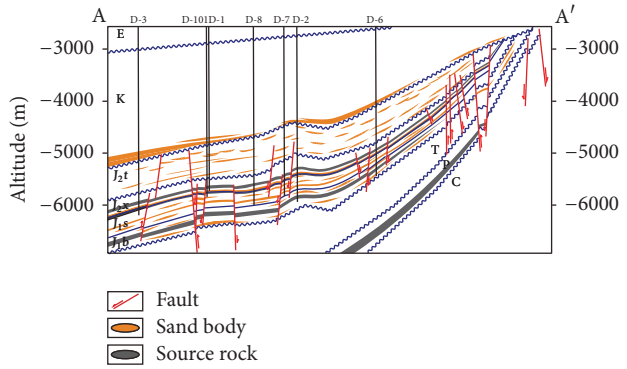

Figure 2: Schematic structural section crossing the studied wells.

formed as a result of the uplift of the Bogda Mountains at the southern margin of the basin since the Paleogene [24]. The Jurassic strata are relatively flat lying or dip gently to the southwest with a dip angle of 2-3° (Figure 2). Most of the observed faults are northeast-directed and east-west-directed normal faults confined to the Jurassic strata (Figures 1(b) and 2). Throw of the fault is generally tens to hundreds of meters and strike length is less than 2 km. These normal faults and deep reversed faults, in some localities, show a flower structure (Figure 2).

The central basin contains Carboniferous to Quaternary sediment fills up to 10 km thick (Figure 3). Rather than attempting an encyclopedic coverage of all the sediments, here, we only summarize general depositional evolution of the Jurassic succession. During the Early Jurassic and early Middle Jurassic period, the central basin was an intracontinental shallow lacustrine basin under the low-amplitude oscillating tectonic regime. Depositional facies identified in the central basin include alluvial fan and fluvial, deltaic, and lacustrine facies [25, 26]. The deposits are typical of a coal-bearing succession and consist of conglomerates, sandstones, and mudstones (Figure 3). Due to the Early Yanshanian orogeny, the lacustrine area began to shrink rapidly during the late Middle-Late Jurassic period. Fluvial, deltaic, and shallow lacustrine facies are included. The deposits are sandstones and mudstones (Figure 3). The contact between the Toutunhe Formation and the underlying Xishanyao Formation is unconformable. The Toutunhe Formation has local erosions, and the Upper Jurassic succession is entirely absent (Figure 3).

Previous exploration and geochemical studies indicate that the Fukang Sag contains four sets of potential source rocks (i.e., Carboniferous, Permian, Triassic, and Jurassic) (Figure 3). Among these source rocks, most discovered hydrocarbons in the Jurassic strata are generally believed to be originated from both the Permian and Jurassic source facies [27–29]. As these source rocks are deeply buried and not easily penetrated by the drill, previous published organic geochemistry studies have been almost entirely restricted to the northern and eastern slope of the sag [29, 30]. The Lower Permian Pingdiquan Formation contains deep lacustrine black mudstones, oil shales, and dolomitic mudstones with a total thickness of 50–650 m [30]. The mudrocks have total organic carbon (TOC) contents ranging from 0.5 to 10.2%. The organic matter is of type I-II kerogen with vitrinite reflectance (Ro) values of 1.2–2.0% [29]. It can be inferred that the source rocks are mature to over mature towards the sag center [30]. The source rocks in the Lower Jurassic and lower Middle Jurassic succession are composed of lacustrine-swamp deep gray mudstones and carbargilites interbedded with thin coal-beds. The mudstones have a total thickness of up to 500 m [30]. The TOC contents range from 0.3 to 3.7%. The organic matter is of type II-III kerogen with Ro values of 0.6–1.0% [29]. The Badaowan Formation's source rocks are of better quality than the Sangonghe and Xishanyao Formation. It is speculated that these source rocks are mature to highly mature towards the sag center [30].

In the Fukang Sag, the Toutunhe Formation's deposits were derived from Kelameili Mountains in the northeast and Bogda Mountains in the south [31–33]. During deposition of the Toutunhe Formation, the study area witnessed a variety of depositional environments ranging from shallow lacustrine through to delta to meandering fluvial system with a total thickness of 700–900 m [33]. The formation can be subdivided into three lithological units (Figure 4). The lower unit (J_{1t3}) consists of grayish-green mudstones and siltstones interbedded with very fine- to fine-grained sandstones. The middle (J_{1t2}) unit includes grayish-green very fine- to fine-grained sandstones, siltstones, and mudstones. The upper unit (J_{1t1}) comprises mainly greyish-brown gravel-bearing medium-grained sandstones, fine-grained sandstones, very fine-grained sandstones, and interlaminated siltstones and mudstones. The Lower Cretaceous mudstones are widely distributed with a total thickness of 140–180 m and can act as the main regional seals for the Jurassic hydrocarbon plays.

3. Samples and Methods

Cores were logged and sampled from the D-1, D-2, D-3, D-6, D-7, and D-8 wells (Figure 4). The specific lithofacies and depositional facies associations of the sandstones were defined based on core description (proportion of sand to shale, bed thickness, grain size, degree of bioturbation and deformation, sedimentary structure, presence of bioclasts and mudstone intraclasts, carbonate cement distribution, etc.). This was combined with wireline logging interpretation to delineate the overall depositional environments for the Toutunhe Formation. All cores were examined under ultraviolet (UV) light for reservoir properties (oil saturation, oil immersion, oil patch, fluorescence, and no show).

Twenty-eight conventional core samples were selected to represent the various depositional facies and lithofacies and the different reservoir properties (Figure 4). Mineralogical, stable carbon and oxygen isotope, and fluid inclusion analyses were performed at the Institute of Geology and Geophysics, Chinese Academy of Sciences, Beijing, China.

All samples were impregnated with blue epoxy resin under vacuum to indicate porosity prior to preparing polished thin sections. Sandstone petrographic compositions were quantified by 300-pointed modal analysis. In addition, the thin sections were studied to identify growth occurrence and habits of interstitial diagenetic minerals and to define

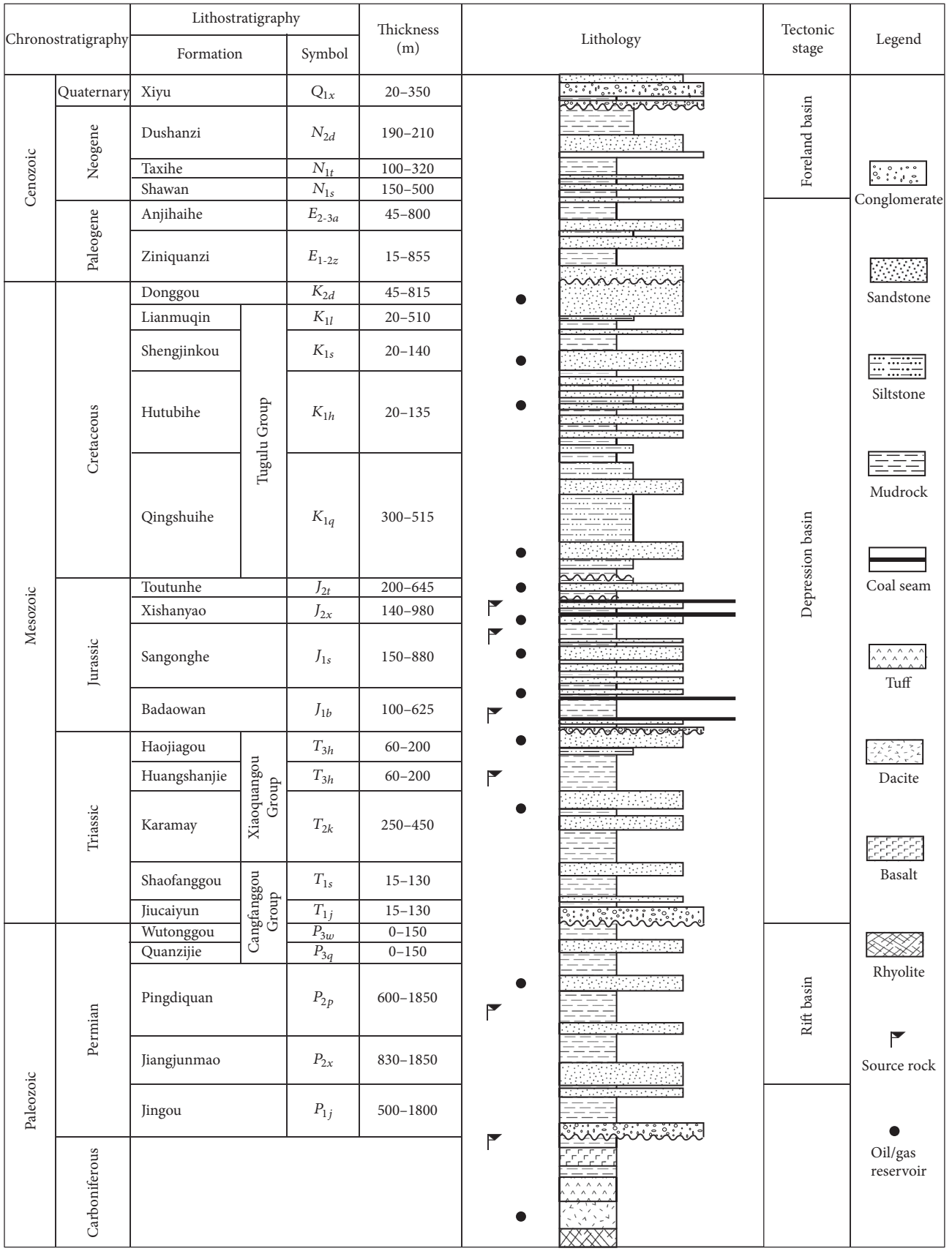

Figure 3: Generalized stratigraphic column of the central Junggar Basin. Tectonic stages refer to Wu [22] and Zhao [23].

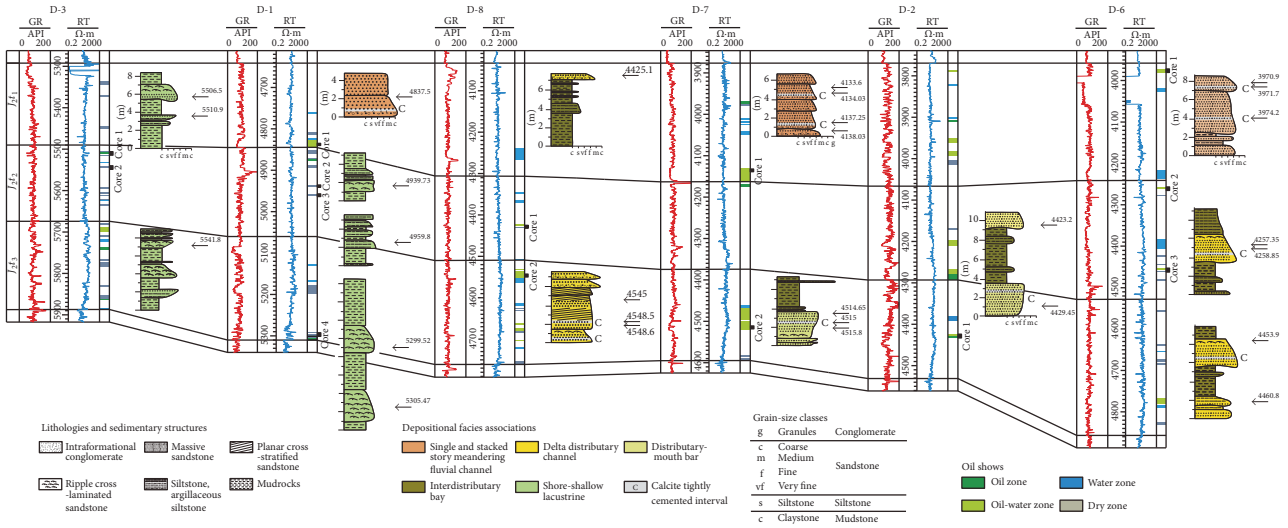

FIGURE 4: Wireline logs of the Toutunhe Formation in the studied wells showing sample depths. Only the point-counted samples are included. Depositional facies associations and lithofacies are interpreted based on core description. Calcite tightly cemented intervals are shown. GR/API: natural gamma-ray log; RT/Ω·m: formation true resistivity.

textural relationships between different cements. Cathodoluminescence (CL) observations were made using a Relion III cold-cathode device at beam voltages of up to 15 keV and 500 μA. To further determine their textural relationships, selected samples were examined using a high-resolution field-emission Nova NanoSEM 450 scanning electron microscope equipped with an integrated analysis system of the Oxford Aztec Energy Dispersive X-ray Spectrometry (EDS) and electron backscatter diffraction (EBSD). Carbon-coated thin sections were mounted on gold grids. All backscatter electron (BSE) images were acquired at 20 keV at a working distance of 5–8 mm. EDS was used for qualitative identification of minerals.

Fourteen samples containing a single generation of calcite cement (either early or late) were selected for carbon and oxygen isotope analysis. The samples were ground to >200 mesh and then soaked overnight in 3% sodium hypochlorite to remove organic matter. Subsequently, the powder samples were reacted with 100% phosphoric acid at 25°C for 4 hours, and CO_2 was extracted and analyzed. The entire process was finished using a Finnigan Delta S mass spectrometer. Oxygen isotopic compositions were calculated using a phosphoric acid-CO_2 fractionation factor of 1.0125 at 25°C. All results were represented in standard notation relative to PDB standard. The reproducibility of duplicate analyses generally was better than ±0.2%.

Nine samples were collected to prepare 100 μm thick doubly polished sections for petrographic observation and microthermometric measurement of fluid inclusions. Petrography of pore bitumen (free oils and solid bitumens) and fluid inclusion and fluid inclusion assemblages were firstly examined using a Nikon 80I microscope under both transmitted and UV light. The wavelength of the emission fluorescence is greater than 420 nm. Homogenization temperature measurement of fluid inclusions was carried out using a calibrated Linkam THMSG600 heating-freezing stage. A step-heating and temperature cycling technique [35] was adopted to record the homogenization temperatures. The precision is ±0.1°C. Fluids inclusions displaying textural or microthermometric evidence for stretching, necking down, leakage, or decrepitation were excluded from the study.

4. Results

4.1. Core Description. Sedimentological description of all cores from six wells with a total length of 53.5 m has been done (Figure 4). Five depositional facies associations of the sandstones have been distinguished: (1) single and stacked story meandering fluvial channel, (2) delta distributary channel, (3) distributary-mouth bar, (4) interdistributary bay, and (5) shore-shallow lacustrine facies association. These facies associations have been identified based on core sections and well log data and are briefly described as follows. Single and stacked story channels are up to 5 m thick, fining-up units ranging mainly from blocky gravel-bearing medium- to very fine-grained sandstones, with minor siltstone and mudstone laminas. The meandering channel facies association dominates the whole upper Toutunhe Formation in the study area. Delta distributary channels are fine-grained sandstones, grading upwards into siltstones. The individual channel units are up to 3 m and sometimes are erosional-based. Sedimentary structures, in some localities, are blocky lamination at the base, changing gradually upwards into planar cross bedding towards the top of the unit, where current ripple is common. Distributary-mouth bars comprise up to 3 m thick, coarsening-up units from siltstones to fine-grained sandstones. The very fine-grained sandstones often display current ripple. Interdistributary bay sediments are almost mudstones interlaminated with thin and lenticular very fine-grained sandstones and siltstones (10 to 20 cm thick). The sandstones often exhibit plane parallel lamination in which bioclasts are common. Delta distributary channel,

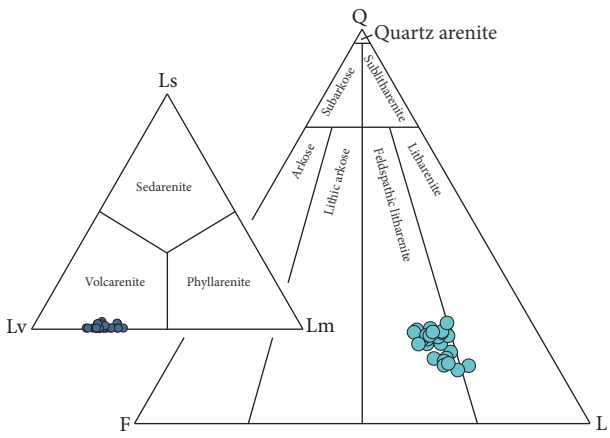

Figure 5: Sandstone QFL triangular classification of the Toutunhe Formation (after Folk [34]).

distributary-mouth bar, and interdistributary bay facies associations are mostly limited to the middle and lower units of the Toutunhe Formation in the D-2, D-6, D-7, and D-8 wells. Shore-shallow lacustrine fills are bioturbated mudstones and interbedded very fine-grained sandstones and siltstones displaying current ripple and plane parallel lamination. Mud intraclast-bearing fine-grained sandstones are seen locally. Patchy pyrite and bioclasts are commonly found. Shore-shallow lacustrine facies association dominates the middle and lower Toutunhe Formation in the D-1 and D-3 wells. In the first three facies associations, calcite commonly forms discrete and tightly cemented concretions (up to 30 cm) embedded in weakly cemented or uncemented sandstones (Figure 6(e)), in particular, in the relatively coarse-grained part of graded sand beds (Figure 4).

4.2. Sandstone Petrology. The Toutunhe Formation's sandstones are very fine- to fine-grained sandstones with the median grain size values of 0.08–0.25 μm. Sorting ranges from moderate to well-sorted. The roundness of detrital sand grains varies from subangular to subrounded.

The sandstones are mostly feldspathic litharenite and litharenite (Figure 5; [34]). The average framework composition is 20.4% quartz, 23.3% feldspar, and 56.4% rock fragments ($Q_{20.4}F_{23.3}L_{56.3}$). The detrital components of the sandstones are dominated by volcanic rock fragments, averaging approximately 36% of the whole rock volume (WRV). The igneous textures recognized in thin sections include lathwork, microlithic, cryptocrystalline, felsitic, and vitric types. Most volcanic rock fragments are composed of euhedral lathwork and microlithic feldspar phenocrysts in the cryptocrystalline groundmass which displays characteristic alteration to clays (Figures 6(a)–6(d)). Metamorphic rock fragments have an average content of about 12%$_{WRV}$ and comprise metamorphosed siltstone, mica schist, slate, and phyllite. Sedimentary rock fragment contents are generally less than 2%$_{WRV}$. They are mostly shale and chert. Some of the lithic fragments are variably altered or deformed and have vague or irregular outlines (Figures 6(a)–6(d)) and termed as "ductile" lithic sand grains. The percentage of the ductile grains is 3–40%$_{WRV}$. Detrital quartz as a fraction of the whole rock averages 17%$_{WRV}$ and is mostly monocrystalline with minor amounts of polycrystalline grains. The polycrystalline quartz features sharp extinction and resorption embayments, which is interpreted as metamorphic origin. Total detrital feldspar averages 20%$_{WRV}$. Plagioclase is the most abundant feldspar type observed, with an average ratio of plagioclase to total feldspar of about 0.7. In addition, detrital clay matrix is locally abundant, up to 8%$_{WRV}$.

4.3. Diagenetic Heterogeneity. Three major sandstone petrofacies have been defined on the basis of texture and detrital compositions, diagenetic features, and pore space properties (i.e., pore abundance and type). Diagenetic features of the three defined sandstone petrofacies are described below.

4.3.1. Ductile Lithic-Rich Sandstone. Ductile lithic-rich sandstones are mainly ripple cross-laminated very fine-grained sandstones (median grain size: 0.08–0.13 μm) that occur in all facies associations (Figure 4). Ductile lithic grains constitute 22–40% of the whole rock in these samples; the contents of detrital matrix are 5–8%$_{WRV}$ (Table 1). Diagenesis of the sandstones is characterized by compaction of easily deformed, clay-rich grains. Ductile grains are severely deformed by mechanical compaction and are squeezed between rigid detrital grains, blocking pore throats (Figures 6(a)–6(c)). In addition to clay minerals almost indiscernible in thin sections, pyrite is an important authigenic phase in the ductile lithic-rich sandstones, ranging from 1%$_{WRV}$ to 3%$_{WRV}$. Pyrite occurs mainly as clusters of cubes in interstitial pores and is an early diagenetic product (Figures 8(f) and 9(h)). The sandstones have no visible thin porosity (Figures 6(a)–6(c)).

4.3.2. Tightly Calcite-Cemented Sandstone. Tightly calcite-cemented sandstones occur in the relatively coarse-grained lithofacies of a graded sand bed (Figure 4), having the median grain size values of 0.17–0.19 μm (Table 1). Tightly calcite-cemented sandstones contain calcite in excess of 20%$_{WRV}$. The calcite cements, which are composed mostly of anhedral calcite crystals (Figure 9(a)), represent a poikilotopic texture and local replacement of framework grains (Figures 6(f) and 6(g)). The calcite precipitated before significant compaction, thereby limiting further diagenetic modifications and resulting in a high intergranular volume. The contents of ductile lithic grains are 3–5%$_{WRV}$ in these samples. The early diagenetic calcite cements exhibit orange-red luminescence emission (Figure 6(g)). The EDS analysis indicates that the calcite has homogeneous almost 100% $CaCO_3$ (Figure 8(g)). The calcite has $\delta^{13}C$ values of −4.3 to −1.4‰ and $\delta^{18}O$ values of −13.4 to −11.2‰ (Table 2). The sandstones have also no visible porosity in thin sections (Figure 6(f)).

4.3.3. Permeable Reservoir Sandstone. Permeable reservoir sandstones are blocky to planar cross-stratified, fine-grained sandstones deposited predominately in the fluvial channel, distributary channel, and distributary-mouth bar facies associations. Ductile grains are less abundant in these samples than in ductile lithic-rich sandstones, ranging from 13%$_{WRV}$

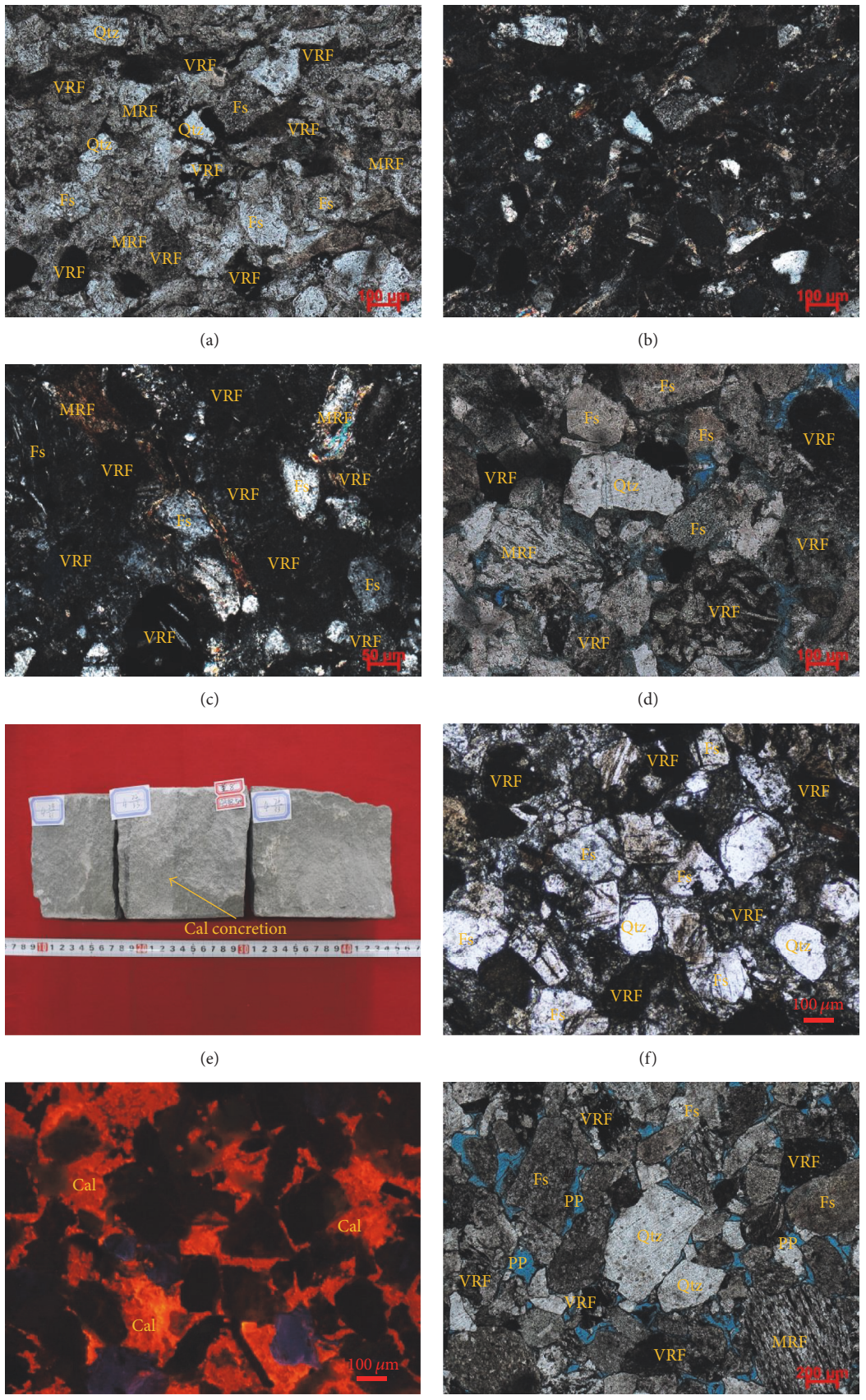

Figure 6: Continued.

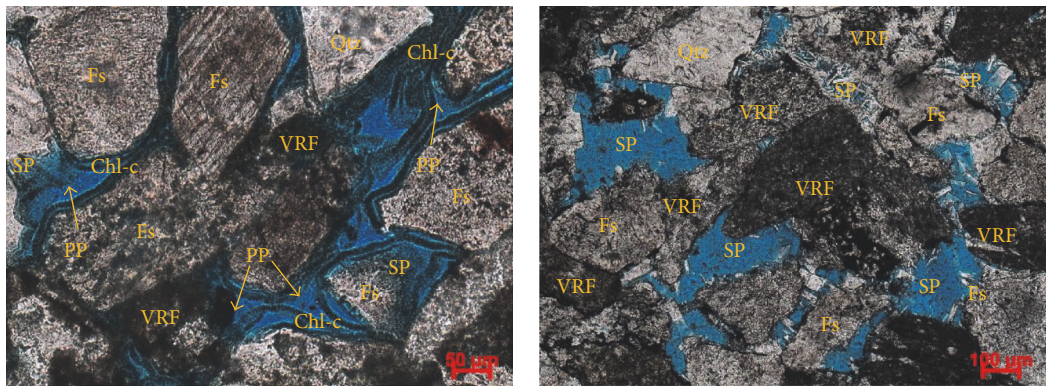

(i) (j)

Figure 6: Thin section images and core photographs of sandstones (pore space is highlighted in blue). ((a) and (b)) Sample 4959.8 m, well D-1, plane-polarized light (PPL), and cross-polarized light (XPL), respectively: the predominance of volcanic rock fragments with various igneous textures. Note that some volcanic rock fragments exhibit a typical characteristic alteration of matrix to clays. (c) Sample 4939.73 m, well D-1, and XPL: volcanic and metamorphic rock fragments deformed between detrital quartz and feldspar grains and smeared on the surfaces of these rigid detrital grains. (d) Sample 4425.1 m, well D-8, and PPL: altered and deformed volcanic and metamorphic rock fragments. (e) Sample 4548.5 m, well D-8: calcite commonly forming white concretions in cores. ((f) and (g)) Sample 4548.5 m, well D-8, PPL, and CL, respectively: calcite representing a poikilotopic texture and local replacement of framework grains. The calcite exhibits orange-red luminescence emission. (h) Sample 4138.03 m, well D-7, and PPL: primary intergranular porosity. (i) Sample 4514.65 m, well D-7, and PPL: primary intergranular porosity and chlorite coats. Partial dissolution along the detrital grain margins is frequently observed. (j) Sample 4837.5 m, well D-1, and PPL: secondary porosity derived from dissolution of detrital grains. Framework grains: quartz (Qtz), feldspar (Fs), volcanic rock fragment (VRF), metamorphic rock fragment (MRF); cement: calcite (Cal), chlorite coat (Chl-c); primary porosity (PP) and secondary porosity (SP).

to 20%$_{WRV}$; the contents of detrital matrix are less than 3%$_{WRV}$ (Table 1). Authigenic minerals include calcite, clay, analcime, anhydrite, barite, quartz overgrowth, albite, and hematite. These cements display a patchy or sporadic texture. Primary intergranular porosity (Figures 6(h) and 6(i)) as counted in thin sections averages 3.9%$_{WRV}$, while secondary porosity averages 1.6%$_{WRV}$ and is affiliated with feldspars and lithic fragments and even minor cements (Figures 6(i), 6(j), and 7(d)).

The calcite contents are low, generally less than 7%$_{WRV}$, and display a rather patchy and local cementation (Figures 7(a), 7(b), and 9(b)). The calcite cements formed after significant compaction and postdated chlorite coats, quartz overgrowths, and feldspar overgrowths or authigenic albite (Figures 8(a) and 8(c)). The calcite displays yellow to orange luminescence (Figure 7(b)). The EDS analysis reveals that the calcite contains Mn in some samples (Figure 8(h)). They have δ^{13}C values of −8.4 to −5.9‰ and δ^{18}O values of −19.0 to −16.4‰ (Table 2).

Chlorite has contents of less than 4%$_{WRV}$. Chlorite cement seems to be facies-related and has been only observed in the distributary channel and distributary-mouth bar facies associations. The chlorite occurs as thick, continuous grain coats and not as pore-filling cement (Figures 6(i), 7(c)–7(e), 8(a), 8(b), and 9(c)). Chlorite coats represent the growth outward from detrital grain surfaces and are absent at points of grain-to-grain contact. Chlorite coats underlie quartz overgrowths, analcime, authigenic albite, barite, and calcite (Figures 7(c)–7(e), 8(a), 8(b) and 9(c)). In addition, minor amounts of illite/smectite are present (Figures 9(d) and 9(e)), particularly in the fluvial channel facies.

There is large variation in the volume of analcime, ranging from 0 to 5%$_{WRV}$. Analcime cements are the most abundant in the fluvial channel facies. The analcime is almost completely extinct and isotropic under crossed-polarized light and shows mainly pore-filling cementation (Figures 7(d), 7(e), 8(e), and 9(e)). Analcime cements are underlain by chlorite coats and replaced by calcite (Figures 7(d)–7(g)) and are intimately intergrown with authigenic albite and illite/smectite clays (Figures 9(d) and 9(e)).

Anhydrite contents are very variable with a maximum of 7%$_{WRV}$. Barite is rare, however, in some samples; up to 2%$_{WRV}$ barite is present. Sulfate cements fill pores in patches and locally replace detrital grains (Figures 7(h), 8(b)–8(d) and 9(f)). Both anhydrite and barite grow over and engulf chlorite coats, quartz overgrowths, feldspar overgrowths, or authigenic albite (Figures 7(i), 7(j), 8(b), 8(c), and 9(f)) and are commonly juxtaposed with some of calcite cements (Figures 7(k), 8(c), and 8(d)).

Authigenic quartz has low contents, generally less than 3%$_{WRV}$. Quartz cements occur as overgrowths on detrital quartz grains (Figures 7(c), 7(i), 8(a), and 9(g)), underlain by chlorite coats (Figure 7(c)) and enclosed by calcite and sulfate cements (Figures 7(i) and 8(a)). The contents of albite cements are less than 2%$_{WRV}$. Albite pore fills and overgrowths occur. Pore-filling albite crystals are euhedral tabular and prismatic-shaped and are underlain by chlorite coats and hematite rims and engulfed by calcite and sulfate cements

Table 1: Point count data summary and sample petrophysical properties. Petrofacies A: ductile lithic-rich sandstone; petrofacies B: calcite tightly cemented sandstone; petrofacies C: permeable reservoir sandstone.

Well	Sample depth (m)	Reservoir properties (class)	Interpretated petrofacies	Core measurement		Thin section porosity (%)			Textural characteristic			Detrital grains (%)			
				Total porosity (%)	Permeability (mD)	Total	Primary	Secondary	Median grain size (mm)	Roundness (class)	Sorting (class)	Quartz	K-Feldspar	Plagioclase	Volcanic rock fragment
D-1	4837.5	Fluorescence	C	8.6	2.09	3.3	2.0	1.3	0.20	SA-SR	M	18.6	5.0	13.5	33.4
D-1	4939.73	No show	A	3.5	0.04				0.10	SA-SR	M	14.0	6.9	14.7	40.5
D-1	4959.8	No show	A	4.5	0.12				0.09	SA-SR	M	11.7	4.5	15.0	42.3
D-1	5299.52	No show	A	5.1	0.07	0.5		0.5	0.12	SA-SR	M	12.8	6.0	15.7	40.0
D-1	5305.47	No show	A	6.3	0.09				0.10	SA-SR	G	13.0	7.3	13.0	40.5
D-2	4423.2	Fluorescence	C	11.8	0.82	4.0	2.3	1.7	0.16	SA-SR	M-G	20.5	4.4	14.0	35.9
D-2	4429.45	Fluorescence	C	14.4	1.70	5.4	4.4	1.0	0.19	SA-SR	M-G	21.9	3.0	13.1	33.0
D-3	5506.5	Fluorescence	C	9.2	1.32	1.8	1.3	0.5	0.15	SA-SR	G	17.0	7.2	16.3	34.0
D-3	5510.9	Fluorescence	C	11.4	2.31	2.0	1.5	0.5	0.15	SA-SR	G	19.4	7.0	14.0	35.3
D-3	5542.8	No show	A	6.3	0.18	0.5		0.5	0.13	SA-SR	M	15.2	8.0	16.3	38.0
D-6	3970.9	Oil stain	C	14.9	1.83	8.7	6.3	2.4	0.16	SA-SR	G	17.0	5.8	15.0	33.6
D-6	3971.7	No show	B	4.5	0.03				0.18	SA-SR	G	18.4	6.0	15.7	30.5
D-6	3974.2	No show	B	4.3	0.06				0.17	SA-SR	G	17.0	7.3	10.2	32.0
D-6	4257.35	Fluorescence	C	13.6	5.16	6.0	4.0	2.0	0.19	SA-SR	G	18.5	7.0	13.5	35.0
D-6	4258.85	Fluorescence	C	11.7	2.79	7.5	4.5	3.0	0.20	SA-SR	G	18.5	6.0	14.0	33.8
D-6	4453.9	No show	A	5.3	0.15				0.11	SA-SR	G	14.7	5.8	15.0	39.4
D-6	4460.8	No show	A	4.5	0.09				0.08	SA-SR	M	12.6	3.0	13.8	42.4
D-7	4133.6	Fluorescence	C	10.3	0.57	3.3	2.3	1.0	0.15	SA-SR	M-G	19.2	7.0	15.0	36.5
D-7	4134.03	Fluorescence	C	12.2	1.66	5.2	3.7	1.5	0.17	SA-SR	M-G	18.0	6.4	16.7	34.7
D-7	4137.25	Fluorescence	C	15.9	11.50	6.2	5.0	1.2	0.21	SA-SR	M	21.5	7.0	13.7	35.0
D-7	4138.03	Fluorescence	C	14.7	3.82	5.3	4.8	0.5	0.20	SA-SR	M-G	20.9	3.0	15.9	34.8
D-7	4514.65	Fluorescence	C	12.5	0.95	7.1	5.1	2.0	0.18	SA-SR	G	18.8	6.0	14.3	36.0
D-7	4515	No show	B	3.5	0.04				0.19	SA-SR	G	17.9	5.5	10.0	31.7
D-7	4515.8	Fluorescence	C	12.9	1.83	8.0	6.0	2.0	0.15	SA-SR	G	15.0	7.0	11.0	38.0
D-8	4425.1	Fluorescence	C	13.7	5.42	7.5	5.0	2.5	0.25	SA-SR	M-G	21.0	8.7	14.7	29.7
D-8	4545	Fluorescence	C	12.9	1.33	5.0	3.5	1.5	0.18	SA-SR	G	19.0	7.4	15.0	32.5
D-8	4548.5	No show	B	3.3	0.05				0.17	SA-SR	M-G	16.5	7.0	8.0	32.4
D-8	4548.6	Fluorescence	C	13.0	1.86	6.0	4.0	2.0	0.17	SA-SR	G	17.4	6.0	13.6	34.0

Table 1: Continued.

Well	Sample depth (m)	Detrital grains (%)						Authigenic minerals (%)							
		Metamorphic rock fragment	Sedimentary rock fragment	Micas	Chert	Ductile grain	Detrital matrix	Albite	Quartz overgrowth	Chlorite	Calcite	Analcime	Anhydrite	Barite	Pyrite
D-1	4837.5	10.1			1.0	13.8	1.5	2.0	1.0		1.0	3.5	4.0	2.0	
D-1	4939.73	13.3		2.0		32.0	6.3								2.3
D-1	4959.8	13.0	1.0	1.5		35.0	8.0								3.0
D-1	5299.52	12.3	1.0	2.0		28.3	7.5				tr.				1.7
D-1	5305.47	12.5		2.2		25.7	8.0								3.0
D-2	4423.2	13.0	0.5			19.1	2.2			4.0	1.5		tr.		
D-2	4429.45	15.3		0.7		18.8	3.5	0.5		3.0		tr.	0.5		
D-3	5506.5	10.5			0.5	16.7	2.3		2.0		1.4		7.0		
D-3	5510.9	11.7				15.2	1.5		1.8		2.0		5.0	0.3	
D-3	5542.8	15.7		0.8		21.9	5.0								1.0
D-6	3970.9	8.3			0.3	13.5	1.0		1.5		2.2	5.0	tr.	1.6	
D-6	3971.7	9.4				5.0	0.5				20.0				
D-6	3974.2	11.5				3.0	1.0				22.0				
D-6	4257.35	9.0				14.9	1.8				6.0	2.7	tr.	0.5	
D-6	4258.85	11.9				13.1			1.0		6.8	0.5			
D-6	4453.9	13.1	1.5	2.0		25.1	5.7				tr.				2.8
D-6	4460.8	14.2	1.0	2.3		40.0	7.7								3.0
D-7	4133.6	12.0				20.0	3.4		1.0		0.5	2.0			
D-7	4134.03	14.0		0.5		19.0	2.0		0.5		0.5	1.5			
D-7	4137.25	12.0	0.5		0.5	15.6	1.5	0.5			0.7	1.0	tr.		
D-7	4138.03	15.6	1.0			16.2	1.0				0.5	2.0			
D-7	4514.65	10.3		0.5		18.1	2.0	1.0		2.7	0.3	1.0			
D-7	4515	11.9				4.0					23.0				
D-7	4515.8	12.5			1.0	18.9	3.0			3.5	0.5	0.5			
D-8	4425.1	15.0				12.7		0.5	0.5		0.5	2.0			
D-8	4545	14.5	1.0			19.8	2.0		2.4		1.2				
D-8	4548.5	10.8		0.5		5.0					24.8				
D-8	4548.6	15.5				15.0	3.2	0.5		3.3		0.5	tr.		

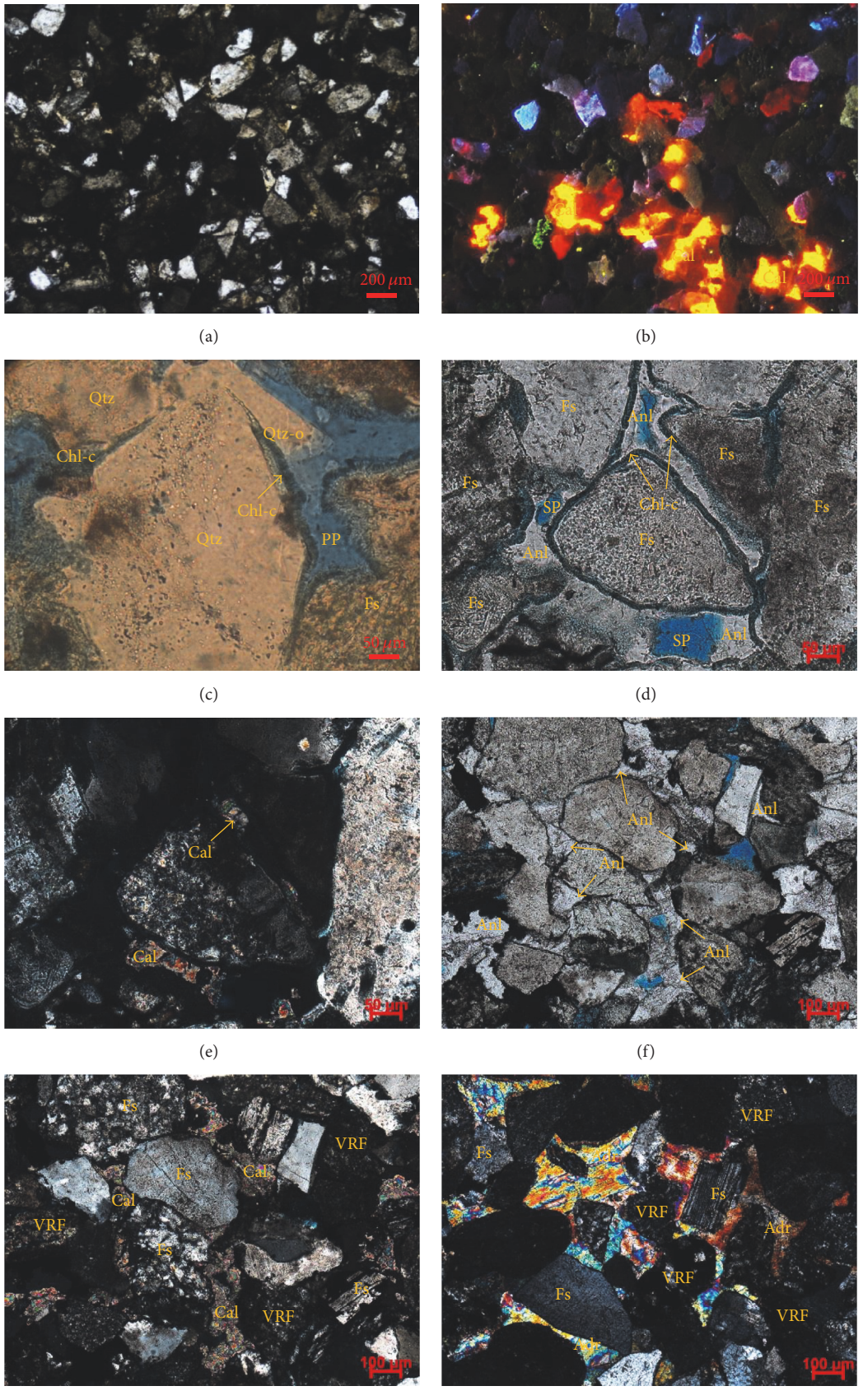

Figure 7: Continued.

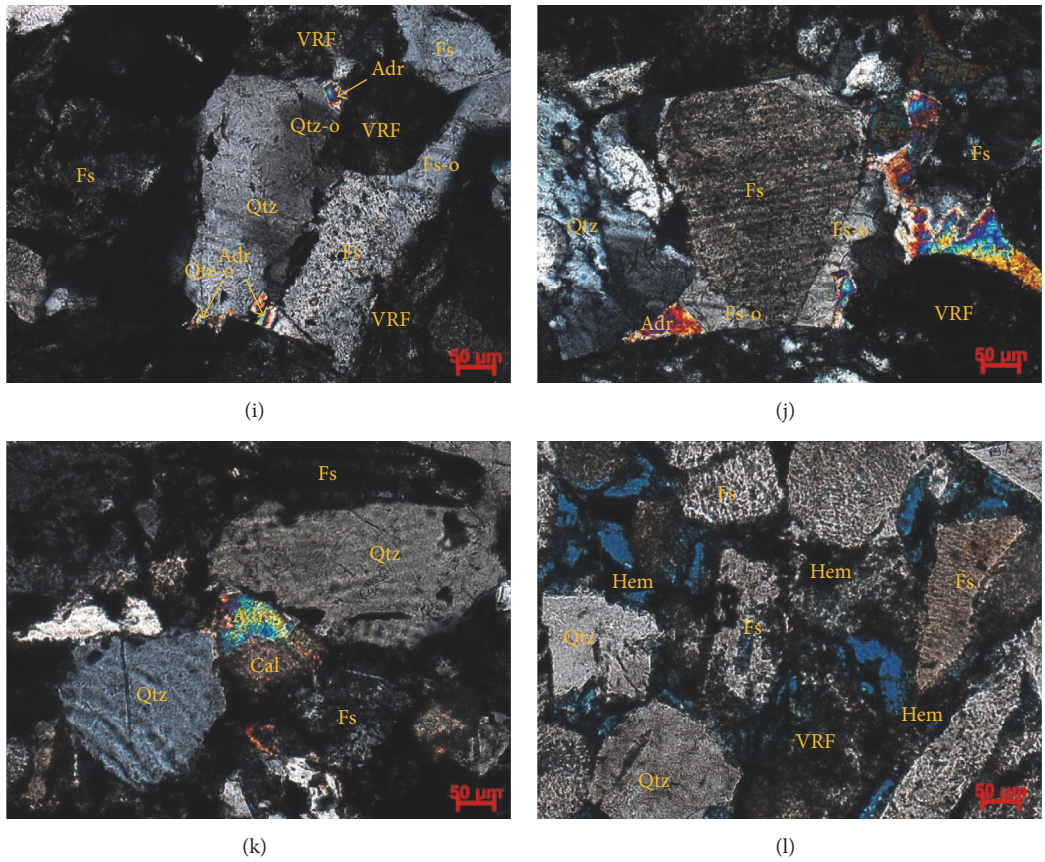

Figure 7: Thin section images of sandstones (pore space is highlighted in blue). ((a) and (b)) Sample 4133.6 m, well D-7, PPL, and CL, respectively: calcite displaying a rather patchy and local cementation and having yellow to orange luminescence. (c) Sample 4429.45 m, well D-2, and PPL: quartz overgrowth precipitated on a detrital quartz grain where there is a break in the continuity of the chlorite coat. ((d) and (e)) Sample 4514.65 m, well D-7, PPL, and XPL: partially dissolved analcime postdating chlorite coats and replaced by calcite. ((f) and (g)) Sample 4258.85 m, well D-6, PPL, and XPL: partially dissolved analcime replaced by calcite. (h) Sample 4837.5 m, well D-1, and XPL: anhydrite cements filling pores in patches and locally replacing detrital grains. (i) Sample 5506.5 m, well D-3, and XPL: quartz overgrowths engulfed by anhydrite. (j) Sample 4837.5 m, well D-1, and XPL: feldspar overgrowths overlain by anhydrite. (k) Sample 5506.5 m, well D-3, and XPL: anhydrite cements commonly juxtaposed with some of calcite cements. (l) Sample 4133.6 m, well D-7, and PPL: hematite occurring as very thin rims around detrital grains. Framework grains: quartz (Qtz), feldspar (Fs), volcanic rock fragment (VRF); cement: calcite (Cal), chlorite coat (Chl-c), analcime (Anl), anhydrite (Adr), quartz overgrowth (Qtz-o), feldspar overgrowth (Fs-o), and hematite (Hem); primary porosity (PP) and secondary porosity (SP).

(Figures 8(b), 8(c), 9(c), 9(d), and 9(f). The albite crystals, in some samples, have been observed to be closely associated with analcime and illite/smectite clays (Figure 9(d)).

Hematite occurs in trace amounts as very thin rims around detrital grains (Figures 7(l) and 8(c)). The grain-riming hematite is generally absent at points of grain-to-grain contact, indicating that it is not syndepositional precipitation. Precipitation of the iron oxides likely occurred from general phreatic oxidation during the late Jurassic uplift [36].

4.4. Pore Bitumens and Fluid Inclusions. Oil shows are localized in cores, indicating the heterogeneous nature of oil migration in a reservoir. Ductile lithic-rich sandstones and tightly calcite-cemented sandstones do not contain oil shows in cores, pore bitumens, or oil-filled fluid inclusions in thin sections. This suggests that oil charge never occurred in these sandstones. By contrast, permeable reservoir sandstones generally have oil shows in cores. Pore bitumens and oil-filled inclusions are present, indicating that oil charged the sandstones. Therefore, permeable reservoir sandstones have been targeted for study of pore bitumens and fluid inclusions.

4.4.1. Petrography. Abundant pore-free oils and solid bitumens have been found. In contrast to nonfluorescent solid bitumens, pore-free oils have yellow and blue-white fluorescence under UV light. The yellow fluorescence dominates. These pore bitumens mostly fill pores and rare feldspar cleavage planes (Figures 10(a)–10(h)). Oil-stained chlorite coats display a yellow fluorescence (Figures 10(a) and 10(b)), indicating that oil charge postdated the precipitation of chlorite coats.

With respect to oil-filled inclusions, two fluorescence colors, yellow and blue-white, have been observed. Similar to pore bitumens, the dominant fluorescence color is

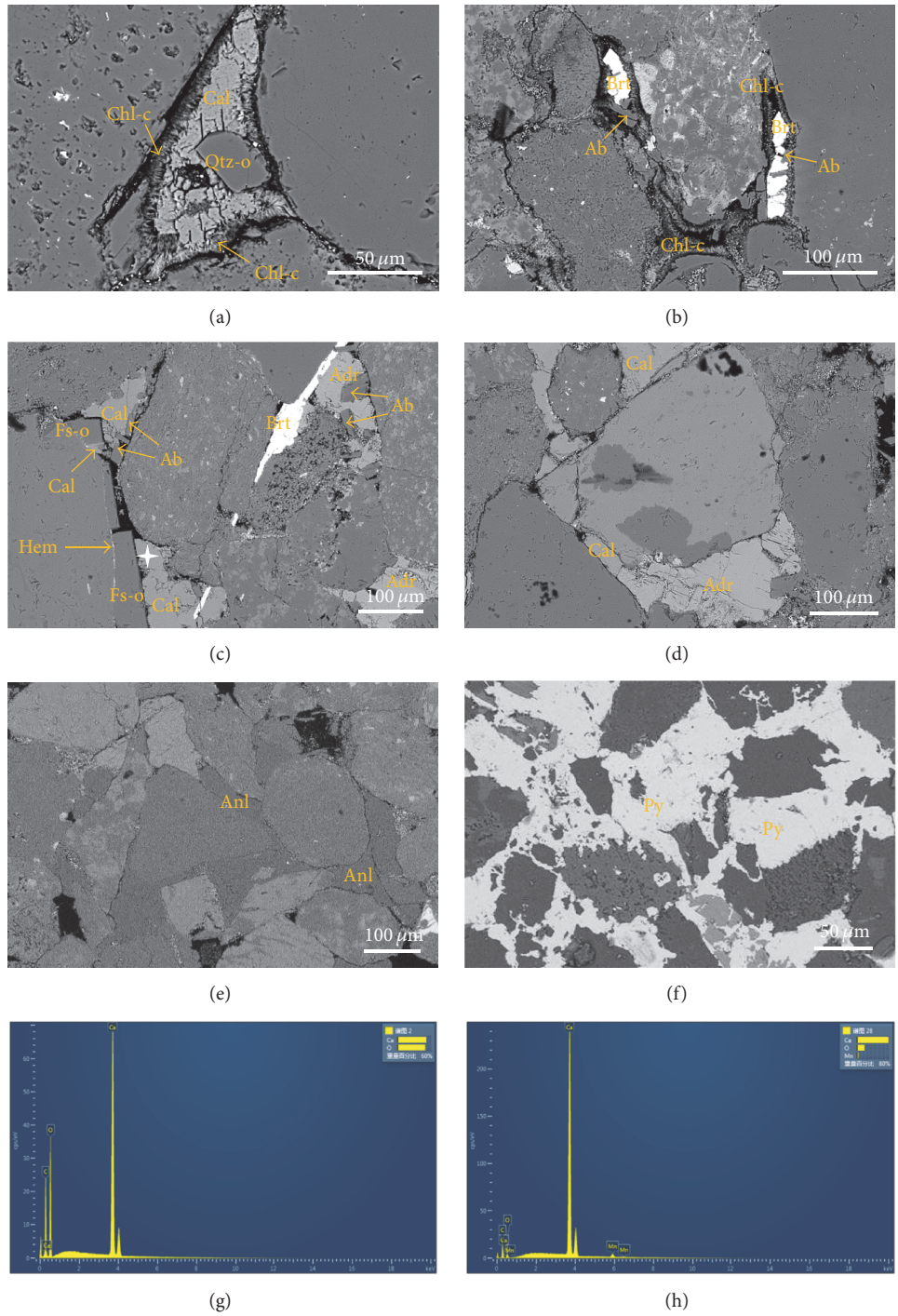

FIGURE 8: SEM BSE images of sandstones. (a) Sample 4514.65 m, well D-7: calcite postdating grain-coating chlorite and quartz overgrowths. (b) Sample 4514.65 m, well D-7: chlorite coats and authigenic albite engulfed by barite. (c) Sample 4837.5 m, well D-1: authigenic albite or feldspar overgrowths postdating hematite rims in contact with detrital grains and engulfed by calcite and anhydrite that are possibly synchronous with barite. (d) Sample 4837.5 m, well D-1: calcite possibly simultaneous with anhydrite. (e) Sample 3970.9 m, well D-6: analcime filling intergranular pores. (f) Sample 5299.52 m, well D-1: pyrite filling intergranular pores and replacing detrital grains locally. (g) Calcite having homogeneous almost 100% $CaCO_3$; the location refers to Figure 9(a). (h) Calcite containing Mn; the location refers to Figure 8(c). Cement: calcite (Cal), chlorite coat (Chl-c), analcime (Anl), anhydrite (Adr), barite (Brt), quartz overgrowth (Qtz-o), feldspar overgrowth (Fs-o), albite (Ab), pyrite (Py), and hematite (Hem).

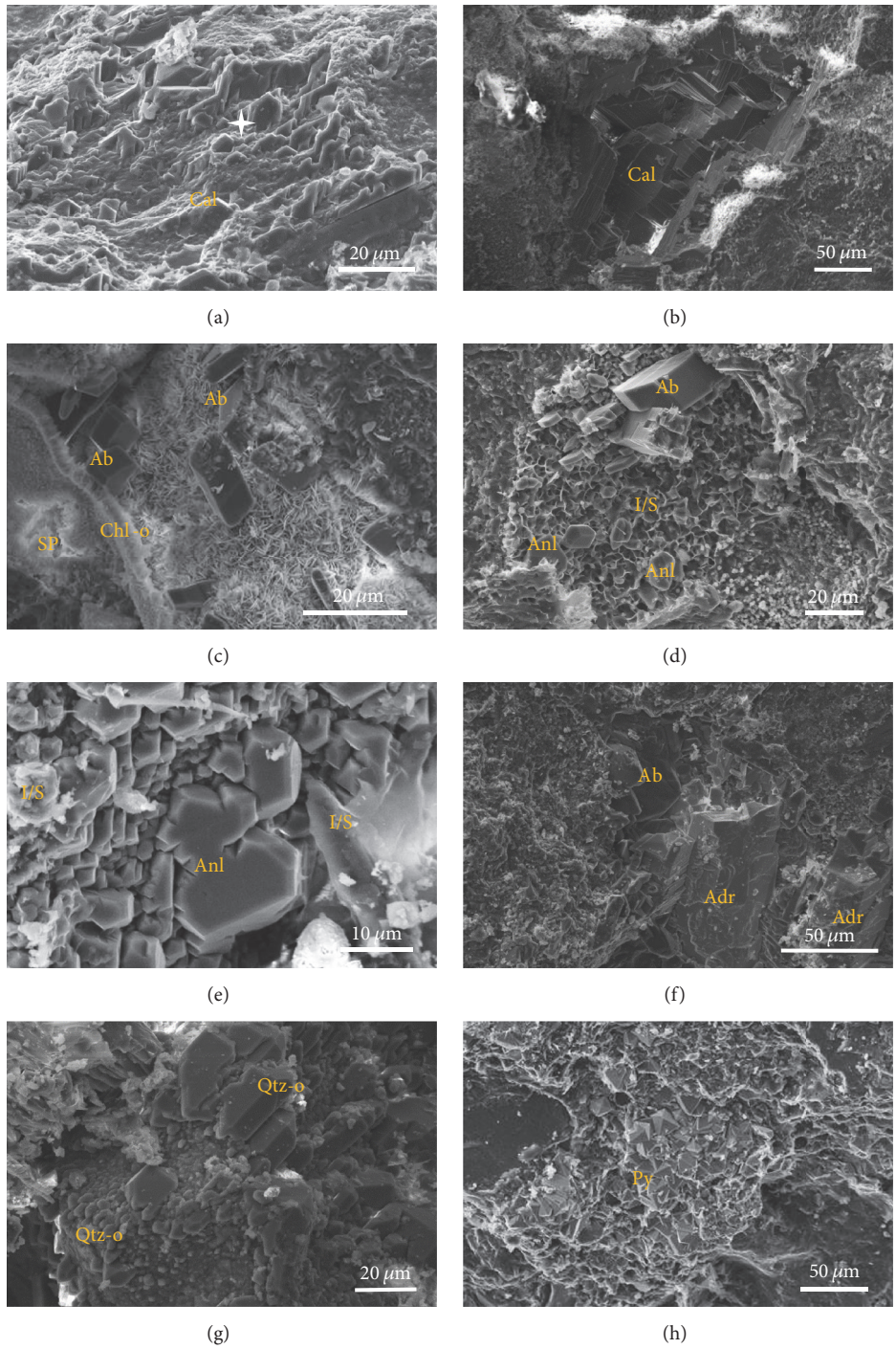

Figure 9: SEM images of sandstones. (a) Sample 4515 m, well D-7: calcite composed mostly of anhedral calcite crystals. (b) Sample 4514.65 m, well D-7: calcite filling pore in patches. (c) Sample 4548.6 m, well D-8: secondary porosity created by complete dissolution of a detrital grain and authigenic albite growing over chlorite coats. Note that relict chlorite coats remain. (d) Sample 4837.5 m, well D-1: analcime and authigenic albite growing over illite/smectite clays. (e) Sample 3970.9 m, well D-6: analcime associated with illite/smectite clays. (f) Sample 5510.9 m, well D-3: anhydrite growing over authigenic albite. (g) Sample 3970.9 m, well D-6: quartz overgrowth. (h) Sample 5299.52 m, well D-1: pyrite filling intergranular pores. Cement: calcite (Cal), chlorite coat (Chl-c), analcime (Anl), anhydrite (Adr), quartz overgrowth (Qtz-o), albite (Ab), and pyrite (Py).

Table 2: Stable carbon and oxygen isotopic compositions of calcite cements in the Toutunhe Formation.

Well	Depth (m)	Calcite type	δ^{13}C (VPDB)	δ^{18}O (VPDB)
D-1	4837.5	Late	−6.0	−18.0
D-2	4423.2	Late	−8.4	−16.4
D-3	5506.5	Late	−6.7	−18.0
D-6	3970.9	Late	−7.8	−18.9
D-6	3971.7	Early	−3.1	−13.0
D-6	3974.2	Early	−4.3	−13.4
D-6	4258.85	Late	−8.4	−17.8
D-7	4133.6	Late	−6.8	−17.9
D-7	4138.03	Late	−7.4	−19.0
D-7	4514.65	Late	−5.9	−18.3
D-7	4515	Early	−4.1	−12.9
D-8	4545	Late	−6.5	−17.4
D-8	4548.5	Early	−1.4	−11.2
D-8	4548.6	Late	−8.3	−16.8

yellow. Oil inclusions are subspherical and elongated in shape, and some irregularly shaped varieties also occur. Oil inclusions are mostly two-phase inclusions containing less than 30 vol.% vapor at 20°C. Three-phase inclusions that contain a hydrocarbon liquid phase (or nonfluorescent solid bitumen), an aqueous liquid phase, and a vapor phase are present occasionally. Most oil inclusions occur within healed microfractures confined to individual quartz grains (Figures 10(i)–10(l)). These oil inclusions generally range in diameter from 3 to 5 μm. In such a case, it is readily easy to find the coexisting aqueous inclusions. A small proportion of oil inclusions also lie in cements (Figures 10(m) and 10(n)), indicating that they were trapped at the time of the precipitation or recrystallization. No oil inclusions have been observed in syntaxial quartz overgrowths, suggesting that quartz precipitated prior to oil arrival. Oil inclusions and associated aqueous inclusions in calcite cements are smaller than within healed microfractures, often less than 3 μm in diameter.

4.4.2. Fluid Inclusion Microthermometry. Oil inclusions and aqueous inclusions in calcite cements are too small to reliably measure their homogenization temperatures, and some of the inclusions appear to have stretched or decrepitated. The aqueous inclusions that are coeval with oil inclusions hosted within quartz microfractures were selected for homogenization temperature measurement. A total of seventy-two homogenization temperature measurements were obtained from twenty-four fluid inclusion assemblages (Table 3). The homogenization temperature values display a bimodal distribution pattern: one population ranges from 80 to 100°C, and the other falls between 110 and 120°C (Figure 11). Noteworthy is the fact that the homogenization temperature values of the aqueous inclusions that are coeval with blue-white fluorescing oil inclusions are marginally lower than those associated with yellow fluorescing ones.

5. Discussion

5.1. Differential Diagenetic Sequences of Sandstones. Fluid inclusion data indicate that two episodes of oil charge took place in permeable reservoir sandstones in the Toutunhe Formation. Different episodes of oil emplacement, here, can be used to distinguish between preoil minerals that formed prior to oil charge, oil-stage minerals whose formation either resulted directly from the charge process or overlapped at least partly in time, and postoil minerals that precipitated after oil arrival in the reservoir. In terms of hydrocarbon migration and accumulation, such a partition is of great significance for understanding the temporal and spatial characteristics of rock-fluid interactions and assessing reservoir quality during the critical period of hydrocarbon charge [17, 18].

Based on textural relationships between authigenic minerals themselves and pore bitumens or oil inclusions, a general paragenetic sequence is presented in Figure 12. The dominant diagenetic features before the first oil charge in permeable reservoir sandstones were mechanical compaction, dissolution of detrital grains, and the formation of hematite rims, chlorite coats, illite/smectite clay, analcime, authigenic albite, and quartz overgrowths. The earliest formed minerals were chlorite coats and hematite rims, which were followed by analcime, authigenic albite, and quartz overgrowths. Most of these diagenetic alterations were controlled by the interaction of subaerial meteoric water with unstable volcanic rock fragments and detrital feldspars. Synchronous with the first oil arrival, quartz cementation was retarded. Anhydrite, barite, and calcite precipitated. When late oil charge occurred, calcite cementation continued. These reactions were controlled by high temperatures and increasingly complicated pore water chemistry arising from the interactions between hydrocarbon fluids and rocks as burial progressed.

In contrast to permeable reservoir sandstones, the compaction of easily deformed, clay-rich grains and associated authigenic clays dominated ductile lithic-rich sandstones before the first oil emplacement. Trace amounts of pyrite precipitated at this period. The ductile compaction continued but reduced with increasing burial. Almost no fluids entered the sandstones later. For tightly calcite-cemented sandstones, calcite cements significantly filled and occluded intergranular pores prior to the first oil arrival. Similar to ductile lithic-rich sandstones, no other diagenetic reactions occurred within the sandstones later.

5.2. Texture-Dependent Mechanical Compaction. The mechanical compaction of lithic sandstones is controlled by the amount and type of lithic fragments [11, 37, 38]. Volcanic rock fragments are the dominant framework component of sandstones in the Toutunhe Formation and are commonly altered. Breakdown of volcanic rock fragments initiated probably during transportation or weathering [38, 39] and continued during burial. When altered by weathering or diagenesis, volcanic rock fragments are extremely ductile [37]. Therefore, the altered volcanic rock fragments are the most important contributor to the mechanical compaction of the sandstones. Upon burial, these ductile grains were deformed between

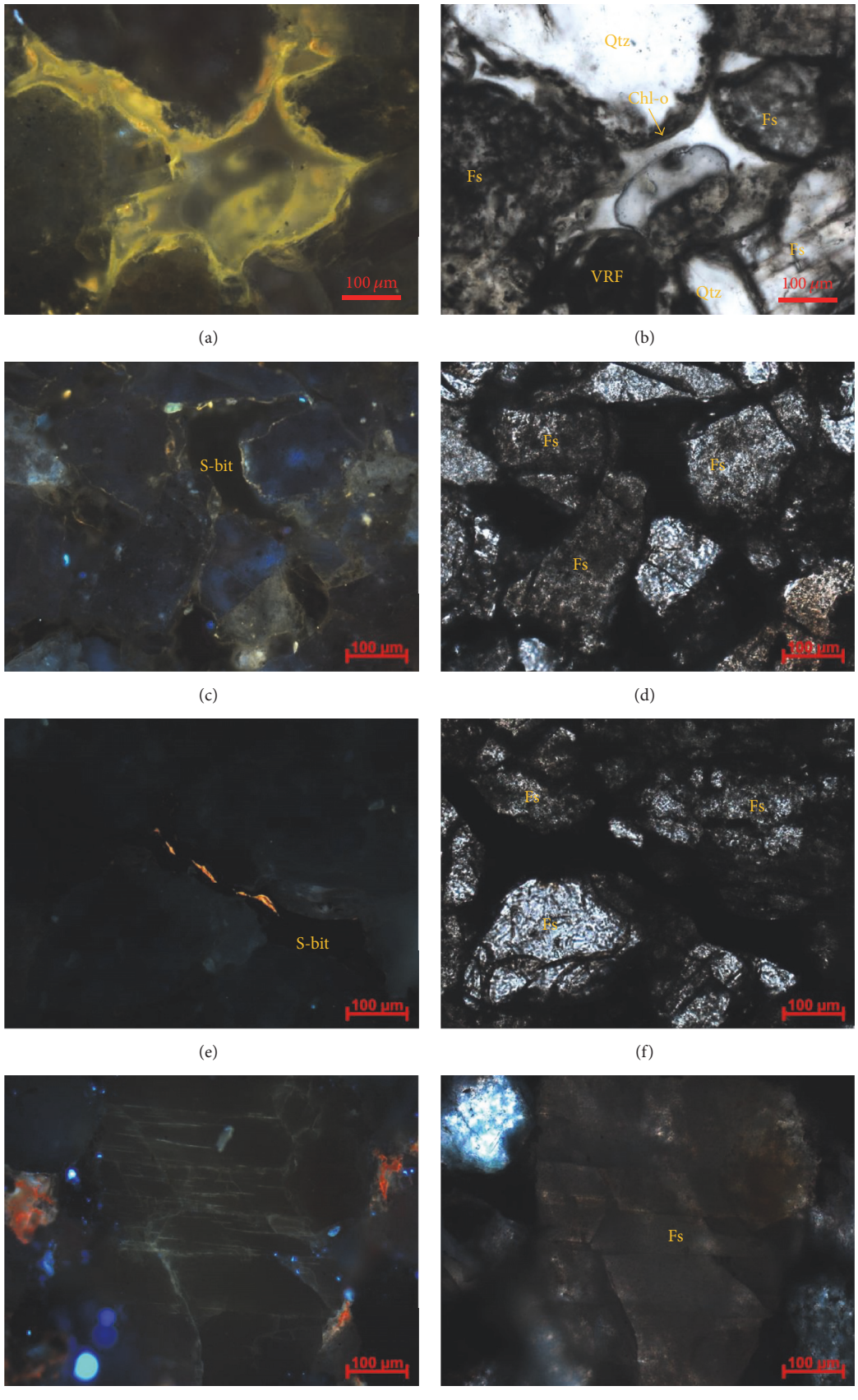

Figure 10: Continued.

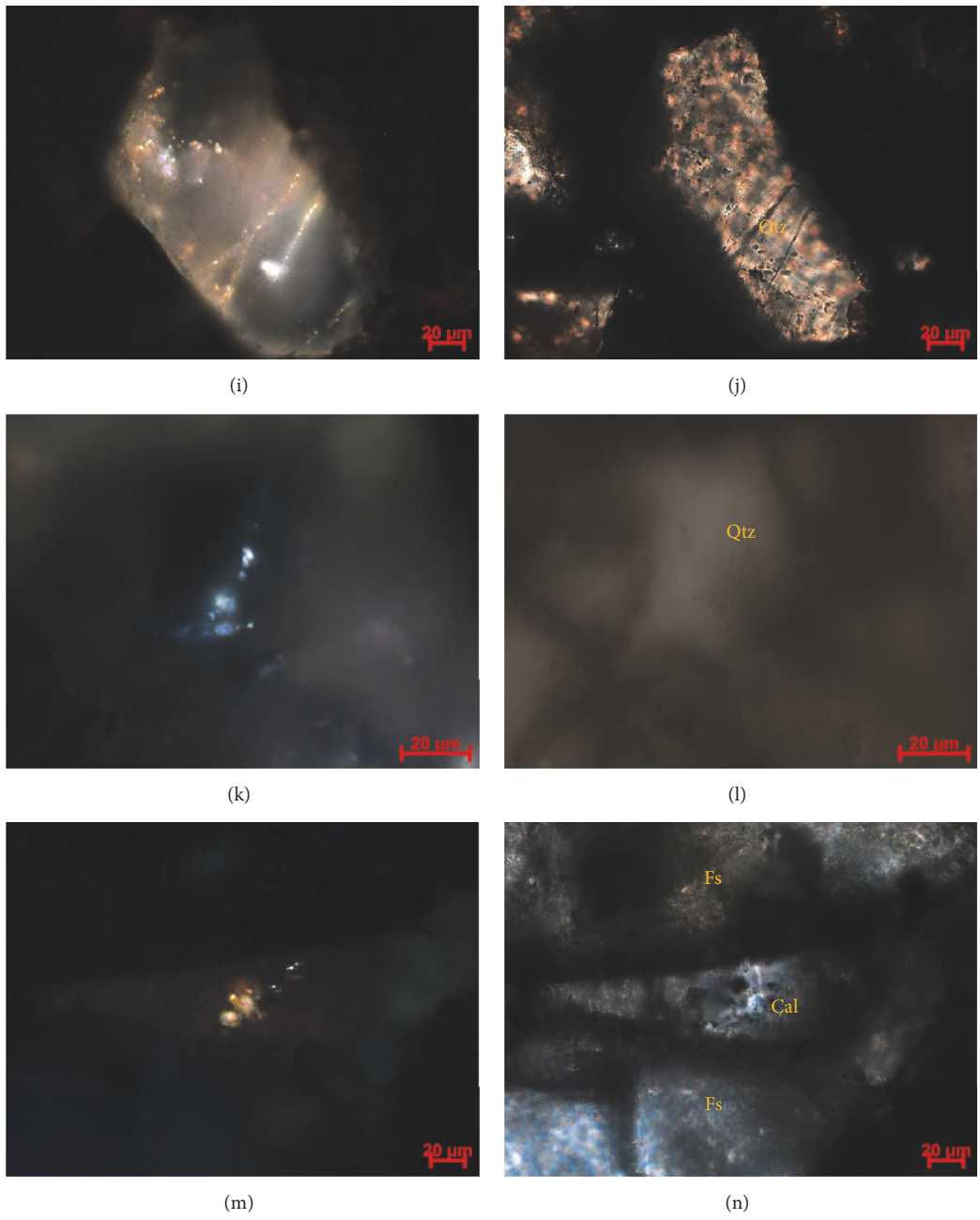

Figure 10: Thin section images of pore bitumens and oil-filled inclusions under transmitted light (a, c, e, g, i, k, m) and UV light (b, d, f, h, j, l, n). ((a) and (b)) Sample 4514.65 m, well D-7: yellow fluorescing oils absorbed over chlorite coats. ((c) and (d)) Sample 4548.6 m, well D-8: pore solid bitumens with yellow fluorescing oils absorbed on walls. ((e) and (f)) Sample 4548.6 m, well D-8: intergranular pore filled with nonfluorescent solid bitumens with yellow fluorescing oils absorbed inside. ((g) and (h)) Sample 4138.03 m, well D-7: blue-white fluorescing oils occurring within cleavage planes of detrital feldspars. ((i) and (j)) Sample 4837.5 m, well D-1: yellow fluorescing oil inclusions occurring along healed microfractures terminating at detrital quartz margin. ((k) and (l)) Sample 3970.9 m, well D-6: blue-white fluorescing oil inclusions healed microfractures in detrital quart. ((m) and (n)) Sample 4258.85 m, well D-6: yellow fluorescing oil inclusions in calcite cements. Framework grains: quartz (Qtz), feldspar (Fs), and volcanic rock fragment (VRF); cement: calcite (Cal) and chlorite coat (Chl-c); solid bitumen (S-bit).

rigid detrital grains. They became smeared over the surfaces of the rigid grains and were squeezed into pore throats leading to significant porosity loss (Figures 6(a)–6(d)). A moderate inverse correlation between porosity and permeability and ductile grain content is presented after excluding the tightly calcite-cemented sandstone samples from the plots in Figure 13, indicating that the ductile compaction is a major cause of porosity loss in the sandstones. Ductile lithic-rich sandstones containing ductile grains in excess of 20%$_{WRV}$ have an average porosity of 5%, ranging from 3.5 to 6.3%,

Table 3: Summary of microthermometry of fluid inclusions.

Well	Sample depth (m)	Reservoir properties (class)	Number of fluid inclusions assemblages	Range of homogenization temperature (°C)
D-1	4837.5	Fluorescence	3	90.7–107.3 (7)
D-2	4429.45	Fluorescence	2	87.5–98.7 (2)
D-3	5510.9	Fluorescence	1	84.3–95.1 (3)
D-6	3970.9	Fluorescence	2	86.6–101.5 (9)
D-6	4258.85	Fluorescence	1	117.2–121.6 (5)
D-7	4133.6	Fluorescence	4	82.3–124.7 (15)
D-7	4137.25	Fluorescence	1	83.2–93.2 (2)
D-7	4514.65	Fluorescence	4	81.6–112.4 (15)
D-8	4545	Fluorescence	6	83.2–113.3 (14)

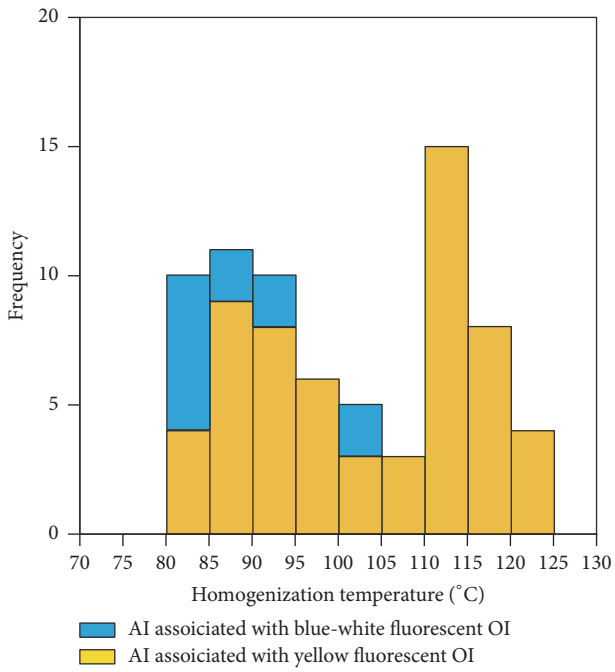

Figure 11: Histograms of homogenization temperatures for aqueous inclusions that are coeval with oil inclusions. Aqueous inclusion (AI) and oil inclusion (OI).

and an average permeability of 0.10 mD, ranging from 0.04 to 0.18 mD. In comparison, permeable reservoir sandstones with less than 20%$_{WRV}$ ductile grain content have an average porosity of 13%, ranging from 8.6 to 15.9%, and an average permeability of 2.76 mD, ranging from 0.57 to 11.50 mD. A threshold value of 20% abundance seems to apply to these ductile grains.

Notably, it is clear from Figure 14 that the ductile grain abundance has a rough negative correlation with grain size. Most of the finer-grained sandstones (ripple cross-laminated) tend to have greater amounts of ductile grains and hence lower porosity and poorer reservoir properties. This suggests that depositional facies and lithofacies were important for predicting ductile components [11, 15, 38].

5.3. Origins of Authigenic Minerals and Their Effects on Reservoir Quality

5.3.1. Chlorite. Chlorite precursor phases and source and transportation of Fe^{2+} irons, almost entirely controlled by paleoclimate, paleosoil, and river system development, significantly affect the formation of chlorite coats [40]. Volcanic rock fragments are the most likely source of Fe^{2+} and Mg^{2+} ions for chlorite coats in the Toutunhe Formation. Five out of seventeen permeable reservoir sandstone samples contain chlorite coats (Table 1), so, while not frequent, they indicate that chlorite coats nonuniformly precipitate in sandstone.

Chlorite coats on quartz grains can prevent pervasive cementation of quartz overgrowths by limiting nucleation sites and inhibit the occlusion of primary intergranular porosity in sandstones [41, 42]. Figure 7(c) illustrates that minor breaks in the continuity of chlorite coats on quartz grains allow precipitation of quartz overgrowth. This is a compelling argument for the preservation of primary porosity by chlorite coats. The sandstones that contain chlorite coats are expected to have relatively high porosity values with a given composition, texture, and burial/temperature. The role of chlorite coats in the preservation of primary porosity, however, is not that important in the Toutunhe Formation. Clay grain coats have no effect on the precipitation of cements other than quartz [42]. Because of the mineralogically immature nature of the sandstones, quartz precipitation is almost volumetrically negligible in the Toutunhe Formation. Therefore, chlorite coats have little impact on primary porosity preservation.

5.3.2. Analcime. The mechanisms reported in the literature which may cause the formation of authigenic analcime in sandstones include direct precipitation from pore water or lake water, reaction of saline and alkaline pore water with detrital silicates, formation from a gel, and alteration of precursor zeolites [43]. In the Toutunhe Formation, no evidence for a precursor zeolite other than analcime has been found. The precipitation of analcime from sodium aluminosilicate gels is generally considered to have been associated with hydrothermal alterations [44]. No hydrothermal gels or other types of gels have been observed. Analcime cements

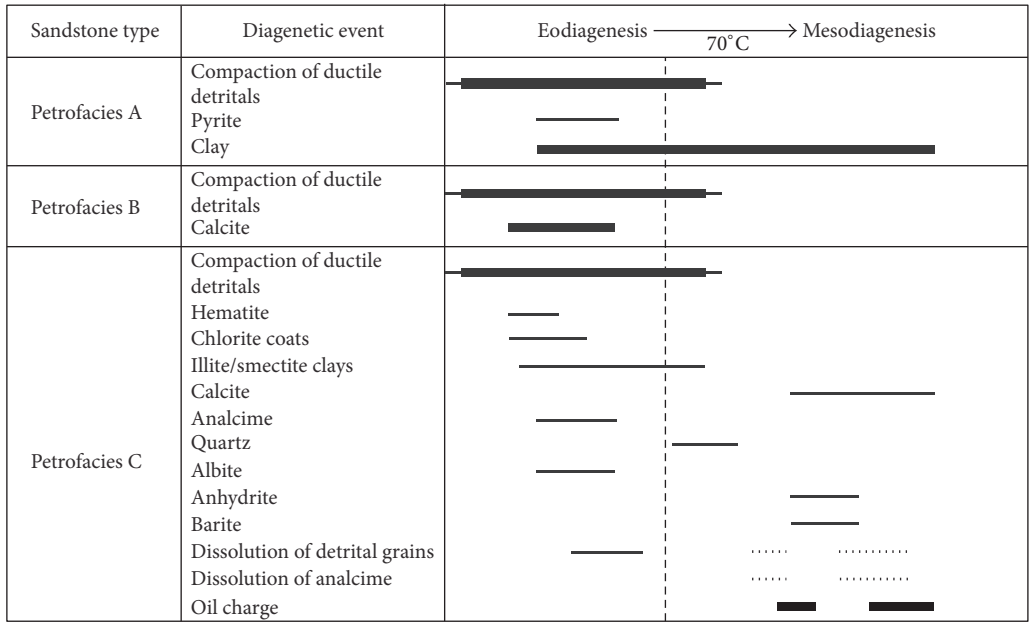

Figure 12: Diagenetic sequences inferred from textural relationships between authigenic minerals and pore bitumens and oil inclusions. Diagenetic regimes used in this study refer to Morad et al. [9]. Petrofacies A: ductile lithic-rich sandstone; petrofacies B: calcite tightly cemented sandstone; petrofacies C: permeable reservoir sandstone.

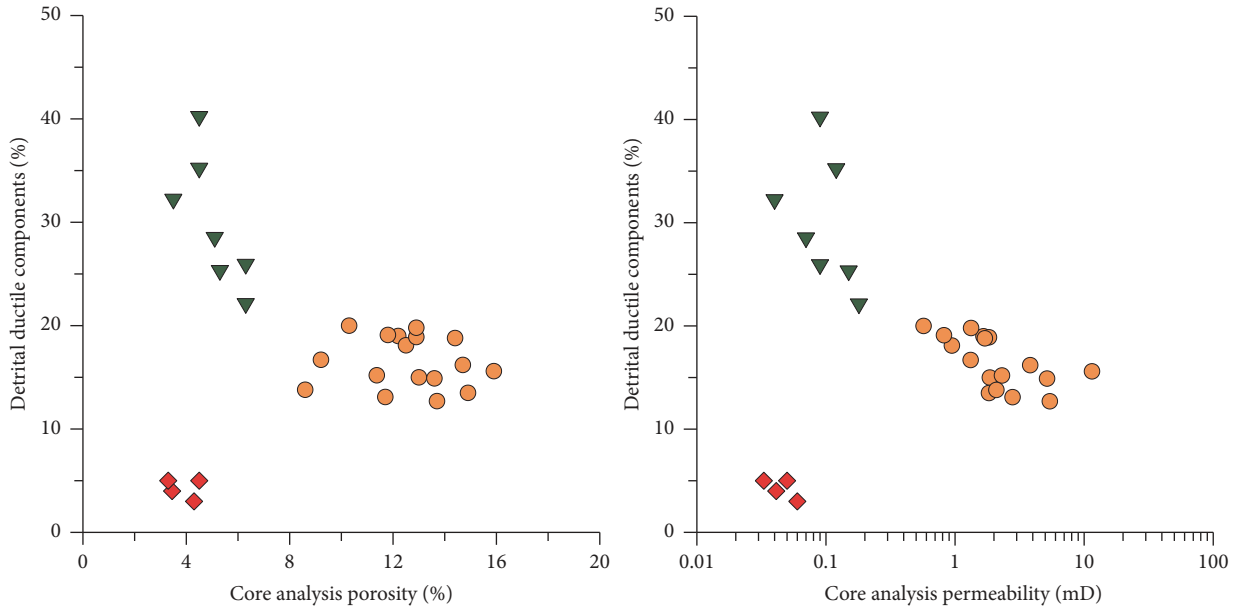

Figure 13: Cross-plot of ductile grain content versus routine core porosity and permeability. Green triangles denote ductile lithic-rich sandstone, red rhombi denote calcite tightly cemented sandstone, and orange circles denote permeable reservoir sandstone.

in sandstones have euhedral, pore-filling, or blocky morphologies, indicating direct precipitation [45]. However, the nonuniform, localized occurrence of the analcime suggests that such a mechanism was not the principal means by which they formed. The reaction of volcanic rock detritus and associated clay derivatives with saline and alkaline pore fluid possibly produced some of the cements [46–48]. In some localities, the analcime cements are closely associated with poorly crystalline clays, possibly some illite/smectite clays (Figures 9(d) and 9(e)).

5.3.3. Calcite. The $\delta^{18}O$ values of calcite in the tightly calcite-cemented sandstones are consistent with the precipitation of early calcite from meteoric water at low temperatures. The

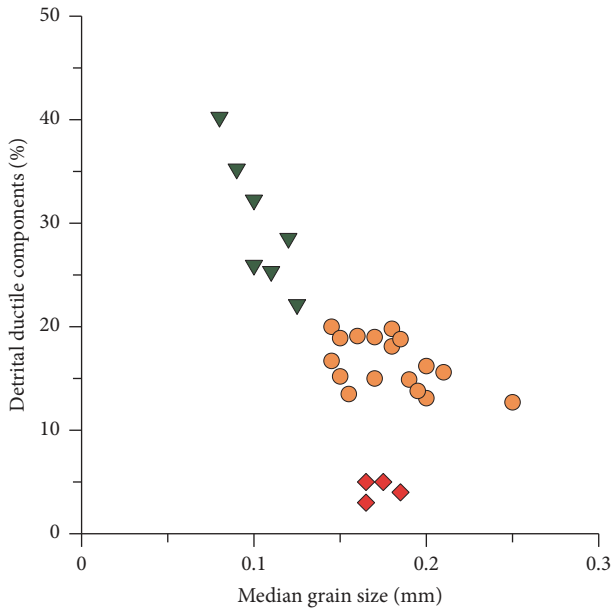

Figure 14: Cross-plot of median grain size versus ductile grain content showing that medium grain size is critical to ductile grain content. Green triangles denote ductile lithic-rich sandstone, red rhombi denote calcite tightly cemented sandstone, and orange circles denote permeable reservoir sandstone.

negative $\delta^{13}C$ values are probably related to a significant carbon contribution from soil-derived bicarbonate or oxidation of organic matter during early diagenesis. The cementation of early calcite, especially in completely cemented sandstones, causes substantial porosity loss. As discussed previously, the calcite forms discrete and tightly cemented concretions in the relatively coarse-grained part of a graded sand bed. This is consistent with an outcrop study from Jiao et al. [49] which indicated that the early calcite concretions occur commonly in the relatively coarse-grained sandstones at the central part of a fining-upward delta distributary channel sequence. They indicated that these concretions, in some localities, are up to 4 m in size and are heterogeneously distributed.

With respect to late calcite cements, the negative $\delta^{13}C$ signature suggests that they were related to the supply of CO_2 derived from decarboxylation of organic matter and Ca^{2+} ions in the formation water. The lower $\delta^{18}O$ values are related to increasing temperatures and fluid-rock interactions during burial diagenesis. The presence of oil inclusions (Figures 10(m) and 10(n)) suggests that, during the formation of the late calcite, the ratio of hydrocarbons to aqueous fluids was high. In addition, the late calcite cements show slight enrichment in Mn^{2+} ions (Figure 6(d)). Cao et al. [50] proposed that Mn^{2+} is most likely derived from volcanic materials in the Junggar Basin and that the enrichment of Mn^{2+} ions in the pore water is closely associated with the dissolution of volcanic materials by "hot" hydrocarbon fluids in the deep Permian source rocks rather than volcanic fragments themselves in shallow sandstones. Therefore, we conclude that some of the late calcite precipitated from a Mn^{2+}-rich hydrocarbon fluid that was introduced from depths into the Toutunhe Formation. It is fair to say that an episode of oil charge, ultimately sourced from the Permian source facies in the deep parts of the Fukang Sag, occurred in the Toutunhe Formation. This is entirely consistent with the analyses of biomarker compositions and geochemical origin of crude oils in the Toutunhe Formation by Hao et al. [51] who indicated that the oils were derived from the Permian and Jurassic source facies in the Toutunhe Formation.

5.3.4. Anhydrite and Barite. A source of SO_4^{2-} and Ba^{2+} ions is required for sulphate cements. These are considered to be outside the Toutunhe Formation. The Permian source rocks contain thin seams of gypsum [52]. These gypsum deposits can spatially provide SO_4^{2-} ions for the sulphate cements. A possible source for Ba^{2+} ions is the underlying Middle-Lower Jurassic coals [53, 54]. Both anhydrite and barite precipitated during late diagenesis, possibly temporally responding to the northeast-southwest trending tilting of the Fukang Sag due to the uplift of the Bogda Mountains since the Paleogene [24]. We tentatively suggest that a great proportion of deep-seated hydrocarbons that were derived from the Permian source facies possibly migrated up along faults from depths and leaked into the Toutunhe Formation. Synchronous with the up-fault migration of deep hydrocarbons, SO_4^{2-} and Ba^{2+} invaded the Toutunhe Formation and were precipitated as barite and anhydrite. Although no oil inclusions have been found in the sulphate cements because of limited thin sections for fluid inclusion study, petrographic evidence indicates that barite and anhydrite cements are possibly simultaneous with late calcite, which contain oil inclusions. Thus the precipitation of the sulphate cements may be lined to oil charge. This further confirms that there was once an episode of charge in the Toutunhe Formation, ultimately sourced from the Permian source facies. The preferential occurrence of the sulphate cements in relatively coarse-grained sandstones may be due to the easier movement of fluids through these sandstones. These sulphate cements generally reduce porosity and permeability but do not completely prevent late flow as they occur in localized patchy areas similar to late calcite.

5.4. Timing of Secondary Dissolution. Determining the timing of secondary dissolution is difficult. Detrital feldspars and volcanic rock fragments are very unstable during near-surface meteoric water flushing [55]. However, the early diagenetic analcime cements, in some samples, have been observed to be partly dissolved (Figures 7(d)–7(g)). Additionally, relic chlorite coats represent delicate textures (Figure 9(c)), suggesting late dissolution. This is because such fabric, if formed relatively early, should have been destroyed or reoccupied by later minerals [56]. Therefore, secondary dissolution most likely continued throughout burial.

A geochemically nearly closed system for burial diagenesis has been accepted [42, 57]. In such a system below the reach of freshwater, the pore water flow is limited and the bulk chemical composition of the sediments does not change significantly. The idea that significant net increases in porosity

may occur during burial diagenesis due to leaching of framework grains by organic acids has mostly been problematic [42, 57]. Furthermore, organic acid quantities are insufficient to significantly influence bulk rock-water equilibria, albeit being present extensively in oilfield formation water [58, 59]. Organic acids may also be neutralized during expelling from source rocks and migration in sandstones [57]. Therefore, we concluded that most of secondary porosity formed by meteoric water influx through the sandstones at shallow burials.

5.5. Effect of Diagenetic Heterogeneity on Fluid Flow. The two sandstone petrofacies, highly compacted, ductile lithic-rich, very fine-grained sandstones, and tightly calcite-cemented sandstones may create permeability barriers or baffles embedded in porous reservoir sandstones. For reasons discussed previously, these permeability barriers are of early diagenetic origin. Depositional environment and lithofacies and the pore water chemistry under near-surface conditions are all key parts in their formation and distribution. These barrier interbeds vary widely in the abundance and occurrence. If they are continuous over large areas in a reservoir, they have a significant effect on fluid flow [6, 19, 60].

Due to reservoir compartmentalization by the intersecting barrier interbeds, oil migration and accumulation in a reservoir are inevitably hindered. An invasion-percolation-based model of oil migration by Luo et al. [18, 19] indicated that oils migrate laterally through a larger fraction of a heterogeneous reservoir than a homogeneous one. Luo et al. [18, 19] thought that not all permeable reservoir compartments separated by the intersecting barrier interbeds act as the pathways for migration or trap for accumulation and a considerable portion of them are filled with formation water. Although the oil-water contact in individual permeable compartments is essentially horizontal, the blocking effect of the intersecting barrier interbeds causes the differences in the oil-water contact between compartments, resulting in an uneven oil-water contact at a reservoir scale. In the Toutunhe Formation, well testing shows that oil and water zones are commonly interbedded; there exists a complex oil-water relationship. Reservoir heterogeneity most likely gives a good explanation for the complex oil-water distribution in the Toutunhe Formation.

In addition, the intra-sand-body barrier interbeds may significantly increase the tortuosity of fluid flow and alter the sweep efficiency, affecting recovery during waterflooding [6, 60].

The study concentrated on reservoir heterogeneity at the core scale. The combination of outcrop study and subsurface data will be used to predict the regional distribution of both the ductile lithic-rich sandstones and tightly calcite-cemented sandstones and thus to characterize reservoir heterogeneity at the macroscale and higher hierarchies. This necessitates single-well heterogeneity characterization and interwell correlation of the area of interest, especially when cores are strictly limited for deep drilling. Therefore, well log responses to these barrier interbeds can be quantified at first. Our future work is to construct regional barrier interbed networks and modeling oil migration.

6. Conclusions

We emphasize that the evaluation of sandstone diagenetic heterogeneity requires systematic examinations of depositional environment and lithofacies that basically determine the primary texture and compositions of sandstones.

Five depositional facies associations of the sandstones have been distinguished based on core sections and well log data: single and stacked story meandering fluvial channel, delta distributary channel, distributary-mouth bar, interdistributary bay, and shore-shallow lacustrine facies association.

The Toutunhe Formation's sandstones consist mostly of feldspathic litharenite and litharenite. Grain size and the abundance of ductile-lithic sand grains are the most important primary detrital controls on diagenesis, porosity, and reservoir properties. These controls operate largely through their effect on mechanical compaction.

Three major sandstone petrofacies have been defined in the Toutunhe Formation. Ductile lithic-rich, very fine-grained sandstones, which occur in all facies associations, are dominated by compaction of easily deformed, clay-rich grains, resulting in a very rapid loss of porosity during burial. Tightly calcite-cemented sandstones occur commonly in the relatively coarse-grained lithofacies of a graded sand bed. By contrast, fine-grained permeable reservoir sandstones, deposited predominately in the fluvial channel, distributary channel, and distributary-mouth bar facies associations, contain relatively less abundant ductile-lithic grains. Various authigenic minerals are present in the relatively coarser-grained sandstone lithofacies with predominately a patchy texture. Chlorite coats only occur in the distributary channel and distributary-mouth bar facies. Analcime and illite/smectite clays are commonly found in the fluvial channel facies. Diagenesis progressed alternately with oil charge, and some diagenetic alterations and oil charge occurred simultaneously. Late diagenetic calcite and sulphate cements may have an indication for oil migration.

Highly compacted, ductile lithic-rich sandstones and tightly calcite-cemented sandstones can create permeability barriers embedded in a porous reservoir, resulting in heterogeneous flow.

Disclosure

The authors accept full responsibility for the ideas and conclusions expressed in the manuscript.

Conflicts of Interest

The authors declare that they have no conflicts of interest.

Acknowledgments

This work was supported by the Strategic Priority Research Program of the Chinese Academy of Sciences (no. XDA14010202) and by the National Natural Science Foundation of China (no. 41372151). The authors are indebted to Mr. Tao Xu at the Shengli Oilfield Company, SINOPIC, for helpful suggestions.

References

[1] F. J. Petrijohn, P. E. Potter, and R. Siever, *Sand and Sandstone*, Springer-Verlag, New York, NY, USA, 1972.

[2] K. J. Weber, "How heterogeneity affects oil recovery," in *Reservoir Characterization*, L. W. Lake and H. B. Carroll Jr., Eds., pp. 487–544, Academic Press, Orlando, Florid, USA, 1986.

[3] C. E. Koltermann and S. M. Gorelick, "Heterogeneity in sedimentary deposits: A review of structure-imitating, process-imitating, and descriptive approaches," *Water Resources Research*, vol. 32, no. 9, pp. 2617–2658, 1996.

[4] P. J. R. Fitch, M. A. Lovell, S. J. Davies, T. Pritchard, and P. K. Harvey, "An integrated and quantitative approach to petrophysical heterogeneity," *Marine and Petroleum Geology*, vol. 63, no. 5, pp. 82–96, 2015.

[5] C. P. North and K. S. Taylor, "Ephemeral-fluvial deposits: Integrated outcrop and simulation studies reveal complexity," *AAPG Bulletin*, vol. 80, no. 6, pp. 811–830, 1996.

[6] S. P. Dutton, C. D. White, B. J. Willis, and D. Novakovic, "Calcite cement distribution and its effect on fluid flow in a deltaic sandstone, Frontier Formation, Wyoming," *AAPG Bulletin*, vol. 86, no. 12, pp. 2007–2021, 2002.

[7] S. Bloch and J. H. McGowen, "Influence of depositional environment on reservoir quality prediction," in *Reservoir Quality Assessment and Prediction in Clastic Rocks*, M. D. Wilson, Ed., vol. 30 of *SEPM Short Course*, pp. 41–57, 1994.

[8] L. F. De Ros, S. Morad, and P. S. G. Paim, "The role of detrital composition and climate on the diagenetic evolution of continental molasses: evidence from the Cambro-Ordovician guaritas sequence, southern Brazil," *Sedimentary Geology*, vol. 92, no. 3-4, pp. 197–228, 1994.

[9] S. Morad, J. M. Ketzer, and L. R. De Ros, "Spatial and temporal distribution of diagenetic alterations in siliciclastic rocks: Implications for mass transfer in sedimentary basins," *Sedimentology*, vol. 47, no. S1, pp. 95–120, 2000.

[10] S. Morad, K. Al-Ramadan, J. M. Ketzer, and L. F. De Ros, "The impact of diagenesis on the heterogeneity of sandstone reservoirs A review of the role of depositional facies and sequence stratigraphy," *AAPG Bulletin*, vol. 94, no. 8, pp. 1267–1309, 2010.

[11] K. L. Milliken, "Diagenetic heterogeneity in sandstone at the outcrop scale, Breathitt formation (Pennsylvanian), eastern Kentucky," *AAPG Bulletin*, vol. 85, no. 5, pp. 795–815, 2001.

[12] S. Henares, L. Caracciolo, C. Viseras, J. Juan Fernández, and L. M. Yeste, "Diagenetic constraints on heterogeneous reservoir quality assessment: a triassic outcrop analog of meandering fluvial reservoirs," *AAPG Bulletin*, vol. 100, no. 09, pp. 1377–1398, 2016.

[13] J. M. Ajdukiewicz and R. H. Lander, "Sandstone reservoir quality prediction: the state of the art," *AAPG Bulletin*, vol. 94, no. 8, pp. 1083–1091, 2010.

[14] K. Bjørlykke, "Relationships between depositional environments, burial history and rock properties. Some principal aspects of diagenetic process in sedimentary basins," *Sedimentary Geology*, vol. 301, no. 3, pp. 1–14, 2014.

[15] Y. Jiao, J. Yan, S. Li, R. Yang, F. Lang, and S. Yang, "Architectural units and heterogeneity of channel resevoirs in the Karamay Formation, outcrop area of Karamay oil field, Junggar basin, northwest China," *AAPG Bulletin*, vol. 89, no. 4, pp. 529–545, 2005.

[16] E. Hammer, M. B. E. Mørk, and A. Næss, "Facies controls on the distribution of diagenesis and compaction in fluvial-deltaic deposits," *Marine and Petroleum Geology*, vol. 27, no. 8, pp. 1737–1751, 2010.

[17] B. Cao, X. Luo, L. Zhang, F. Sui, H. Lin, and Y. Lei, "Diagenetic evolution of deep sandstones and multiple-stage oil entrapment: A case study from the Lower Jurassic Sangonghe Formation in the Fukang Sag, central Junggar Basin (NW China)," *Journal of Petroleum Science and Engineering*, vol. 152, no. 3, pp. 136–155, 2017.

[18] X. R. Luo, L. K. Zhang, Y. H. Lei, C. Z. Hu, H. Shi, and B. F. Cao, "Structural heterogeneity of reservoirs and its implication on hydrocarbon accumulation in deep zones," *China Petroleum Exploration*, vol. 21, no. 1, pp. 28–36, 2016.

[19] X. Luo, C. Hu, Z. Xiao et al., "Effects of carrier bed heterogeneity on hydrocarbon migration," *Marine and Petroleum Geology*, vol. 68, no. 12, pp. 120–131, 2015.

[20] S. J. Ren, C. F. Jiang, Z. K. Zhang, and D. Y. Qin, *The Geotectonic Evolution of China*, Science Press, Beijing, China, 1980.

[21] B. Zhao, "Nature of basement of Junggar Basin," *Xinjiang Petroleum Geology*, vol. 13, no. 2, pp. 95–99, 1992.

[22] Q. F. Wu, "Growth stage, classification of structural units and cause of partial tectonic of Junggar Basin," *Xinjiang Petroleum Geology*, vol. 71, no. 1, pp. 29–37, 1986.

[23] B. Zhao, "Formation and Evolution of Junggar Basin," *Xinjiang Petroleum Geology*, vol. 13, no. 3, pp. 191–196, 1992.

[24] P. L. Li, J. H. Feng, Y. C. Lu et al., *Structure, sedimentation, and petroleum accumulation in the Junggar Basin*, Geological Publishing House, Beijing, China, 2010.

[25] Z. H. Tang, Y. Huang, and H. L. Zhang, "Sedimentary facies and sequences of Jurassic in estern Junggar Basin," *Xinjiang Petroleum Geology*, vol. 18, no. 4, pp. 330–337, 1997.

[26] M. L. Zhang, X. M. Zhu, and Q. Zhang, "Jurassic sedimentary system of east Junggar Basin and its hydrocarbon significance," *Oil Gas Geology*, vol. 21, no. 3, pp. 272–278, 2000.

[27] C. G. Wang, T. G. Wang, J. P. Chen, X. P. Shi, S. Z. Xiang, and T. Jin, "Recognition of crude oil types in the Jurassic Reservoirs of Cainan oilfield, east Junggar Basin," *Petroleum Geology Experiment*, vol. 25, no. 3, pp. 183–189, 2003.

[28] J. P. Chen, C. P. Deng, D. G. Liang et al., "The Cainan Oilfield: a typical mixed crude oil of three-endmember," *ActaSedimentol. Sin*, vol. 22, pp. S91–S97, 2004.

[29] H. Kuang, *Accumulation Regularity of Lithology reservoirs in Jurassic Baijiahai area, Jungar Basin [Ph.D. Dissertation]*, Yangtzi University, Wuhan, China, 2009.

[30] J. Chen, D. Liang, X. Wang et al., "Mixed oils derived from multiple source rocks in the Cainan oilfield, Junggar Basin, Northwest China. Part I: genetic potential of source rocks, features of biomarkers and oil sources of typical crude oils," *Organic Geochemistry*, vol. 34, no. 7, pp. 889–909, 2003.

[31] Q. Zhang, M. L. Zhang, X. M. Zhu, D. K. Zhong, and G. W. Wang, "Analysis of Jurassic sources in east Fukang slope of Junggar Basin," *Xinjiang Petroleum Geology*, vol. 20, no. 6, pp. 501–546, 1999.

[32] J. Jin, H. G. Wen, B. L. Xiang, L. Q. Qi, J. W. Yu, and L. L. Li, "Provenance analysis of Middle Jurassic Toutunhe Formation in eastern Fukang slope, Junggar Basin," *Lithologic Reservoirs*, vol. 26, no. 2, pp. 54–58, 2014.

[33] M. Zhang, J. L. Xiu, L. Chen, and T. Xu, "The provenance system and characteristic of sedimentary evolution of Jurassic Toutunhe Formation in the second and fourth Blocks of central Junggar Basin," *Journal of Oil and Gas Technology*, vol. 36, no. 6, pp. 45–50, 2014.

[34] R. L. Folk, *Petrology of Sedimentary Rocks*, Hemphills, Austin, Texas, USA, 1974.

[35] R. H. Goldstein and T. J. Reynolds, "Systematics in fluid inclusions in diagenetic minerals," *SEPM Short Course*, vol. 31, 1994.

[36] Y.-Q. Jiao, L.-Q. Wu, Y.-C. Lu, and J.-Y. Ren, "Evolution of the Chepaizi-Mosuowan paleo-uplift, Junggar Basin, China: Evidence from diagenesis of late Jurassic red beds," *Journal of China University of Geosciences*, vol. 33, no. 2, pp. 219–226, 2008.

[37] E. D. Pittman and R. E. Larese, "Compaction of lithic sands: experimental results and applications," *American Association of Petroleum Geologists Bulletin*, vol. 75, no. 8, pp. 1279–1299, 1995.

[38] R. H. Worden, M. Mayall, and I. J. Evans, "The effect of Ductile-Lithic sand grains and quartz cement on porosity and permeability in Oligocene and lower Miocene clastics, South China Sea: prediction of reservoir quality," *AAPG Bulletin*, vol. 84, no. 3, pp. 345–359, 2000.

[39] H. Kashiwagi, Y. Ogawa, and N. Shikazono, "Relationship between weathering, mountain uplift, and climate during the Cenozoic as deduced from the global carbon-strontium cycle model," *Palaeogeography, Palaeoclimatology, Palaeoecology*, vol. 270, no. 1-2, pp. 139–149, 2008.

[40] P. J. Dowey, D. M. Hodgson, and R. H. Worden, "Pre-requisites, processes, and prediction of chlorite grain coatings in petroleum reservoirs: a review of subsurface examples," *Marine and Petroleum Geology*, vol. 32, no. 1, pp. 63–75, 2012.

[41] S. Bloch, R. H. Lander, and L. Bonnell, "Anomalously high porosity and permeability in deeply buried sandstone reservoirs: origin and predictability," *AAPG Bulletin*, vol. 86, no. 2, pp. 301–328, 2002.

[42] T. R. Taylor, M. R. Giles, L. A. Hathon et al., "Sandstone diagenesis and reservoir quality prediction: models, myths, and reality," *AAPG Bulletin*, vol. 94, no. 8, pp. 1093–1132, 2010.

[43] R. W. Renaut, "Zeolitic diagenesis of late Quaternary fluvio-lacustrine sediments and associated calcrete formation in the Lake Bogoria Basin, Kenya Rift Valley," *Sedimentology*, vol. 40, no. 2, pp. 271–301, 1993.

[44] R. C. Surdam and H. P. Eugster, "Mineral reactions in the sedimentary deposits of the Lake Magadi region, Kenya," *Bulletin of the Geological Society of America*, vol. 87, no. 12, pp. 1739–1752, 1976.

[45] Q. Gall and R. Hyde, "Analcime in lake and lake-margin sediments of the Carboniferous Rocky Brook Formation, Western Newfoundland, Canada," *Sedimentology*, vol. 36, no. 5, pp. 875–887, 1989.

[46] R. L. Hay, "Silicate reactions in three lithofacies of a semi-arid basin, Olduvai Gorge Tanzania," *Mineralogical society of America*, vol. 3, pp. 237–255, 1970.

[47] Y. S. Sun and Z. Q. Cao, "Characteristics and distribution of Zeolite group minerals in Karamay Oilfeilds," *Xinjiang Petroleum Geology*, vol. 12, no. 3, pp. 253–261, 1991.

[48] S. F. Zhu, X. M. Zhu, X. L. Wang, and Z. Y. Liu, "Zeolite diagenesis and its control on petroleum reservoir quality of Permian in northwestern margin of Junggar Basin, China," *Science China Earth Sciences*, vol. 55, no. 3, pp. 386–396, 2012.

[49] Y. Q. Jiao, S. T. Li, S. G. Yang, and J. L. Chen, "An outcrop study on internal architecture and heterogeneity of lacustrine delta-front sand bodies , Journal of China University of Geosciences," *Earth Science*, vol. 18, no. 4, pp. 441–451, 1993.

[50] J. Cao, W. Hu, S. Yao et al., "Content of reservoir calcite cement: A novel inorganic geotracer of secondary petroleum migration in the structurally complex Junggar Basin (NW China)," *Science China Earth Science*, vol. 37, no. 10, pp. 1358–1369, 2007.

[51] F. Hao, Z. Zhang, H. Zou, Y. Zhang, and Y. Yang, "Origin and mechanism of the formation of the low-oil-saturation Moxizhuang field, Junggar Basin, China: implication for petroleum exploration in basins having complex histories," *AAPG Bulletin*, vol. 95, no. 6, pp. 983–1008, 2011.

[52] L. Kuang, Y. Tang, D. Lei et al., "Formation conditions and exploration potential of tight oil in the Permian saline lacustrine dolomitic rock, Junggar Basin, NW China," *Petroleum Exploration and Development*, vol. 39, no. 6, pp. 700–711, 2012.

[53] J. Gluyas, L. Jolley, and T. Primmer, "Element mobility during diagenesis: Sulphate cementation of Rotliegend sandstones, Southern North Sea," *Marine and Petroleum Geology*, vol. 14, no. 7-8, pp. 1001–1011, 1997.

[54] B. McNeil, H. F. Shaw, and A. H. Rankin, "The timing of cementation in the Rotliegend sandstones of the southern North Sea: a petrological and fluid inclusion study of cements," *Journal of Petroleum Geology*, vol. 21, no. 3, pp. 311–328, 1998.

[55] R. C. Surdam and J. R. Boles, "Diagenesis of volcanogenic sandstones," in *Aspects of Diagenesis*, P. A. Scholle and P. R. Schluger, Eds., vol. 26 of *Special Publication*, pp. 227–247, Society for Sedimentary Geology, Tulsa, USA, 1979.

[56] Z. Tang, J. Parnell, and F. J. Longstaffe, "Diagenesis and reservoir potential of Permian-Triassic Fluvial/Lacustrine sandstones in the southern Junggar basin, northwestern China," *AAPG Bulletin*, vol. 81, no. 11, pp. 1843–1865, 1997.

[57] K. Bjørlykke and J. Jahren, "Open or closed geochemical systems during diagenesis in sedimentary basins: constraints on mass transfer during diagenesis and the prediction of porosity in sandstone and carbonate reservoirs," *AAPG Bulletin*, vol. 96, no. 12, pp. 2193–2214, 2012.

[58] T. Barth and K. Bjørlykke, "Organic acids from source rock maturation: generation potentials, transport mechanisms and relevance for mineral diagenesis," *Applied Geochemistry*, vol. 8, no. 4, pp. 325–337, 1993.

[59] P. D. Lundegard and Y. K. Kharaka, "Distribution and occurrence of organic acids in subsurface waters," in *Organic Acids in Geological Processes*, E. D. Pittman and M. D. Lewan, Eds., pp. 38–69, Springer-Verlag, New York, NY, USA, 1994.

[60] M. D. Jackson and A. H. Muggeridge, "Effect of discontinuous shales on reservoir performance during horizontal waterflooding," *SPE Journal*, vol. 5, no. 4, pp. 446–455, 2000.